

RESEARCH ARTICLE SUMMARY

IMMUNOLOGY

Kupffer cell-like syncytia replenish resident macrophage function in the fibrotic liver

Moritz Peiseler†, Bruna Araujo David†, Joel Zindel, Bas G. J. Surewaard, Woo-Yong Lee, Felix Heymann, Ysbrand Nusse, Fernanda V. S. Castanheira, Raymond Shim, Adrien Guillot, Alix Bruneau, Jawairia Atif, Catia Perciani, Christina Ohland, Priyanka Ganguli Mukherjee, Annika Niehrs, Roland Thuenauer, Marcus Altfeld, Mathias Arrein, Zhaoyuan Liu, Paul M. K. Gordon, Kathy McCoy, Justin Deniset, Sonya MacParland, Florent Ginhoux, Frank Tacke, Paul Kubes*

INTRODUCTION: The local environment is critical for establishing the phenotype of macrophages within a given organ. In the liver, resident macrophages reach out of the sinusoids to receive instructive cues in a niche composed of hepatocytes, endothelial cells, and stellate cells. These cues activate specific transcription factors, which endow these macrophages with Kupffer cell (KC) “identity.” In the sinusoids, KCs perform the critical function of capturing pathogens from the blood by means of specialized receptors, including the complement receptor CR1g. Liver fibrosis and cirrhosis is the common end-stage of various chronic liver diseases, leading to substantial morbidity and mortality in affected individuals. Despite different etiologies, progression is similar, with hepatocyte death and collagen deposition around sinusoids, resulting in the redistribution of blood flow to new and expanded intrahepatic and extrahepatic collateral vessels.

RATIONALE: It remains unclear how fibrotic remodeling of the niche environment affects

the KC compartment. In this study, we used various lineage-tracing models and intravital microscopy to visualize, track, and functionally assess monocytes and KCs in the fibrotic liver environment.

RESULTS: Using the most common mouse model of liver fibrosis—carbon tetrachloride toxicity—we observed profound architectural changes in the liver. This remodeling included a massive increase in collateral vessels and collagen deposition around the sinusoids, which caused KCs to lose contact with their surrounding environment. This, in turn, led to the down-regulation of key transcription factors and membrane proteins such as CLEC4F, CR1g, and TIM-4, which collectively determine KC identity. Although these changes resulted in impaired KC function, the liver continued to act as a major filter of blood-borne bacteria despite the loss of KC identity.

An abundance of monocytes were recruited, and these cells primarily adhered to large intrahepatic vessels through CD44 owing to increased endothelial cell adhesivity driven

by intestinal microbiota. Monocytes formed large clusters within the collateral vessels and began to express KC markers. These monocytes made up a spectrum of structures ranging from clusters of individual cells to fused multinucleated giant cells that collectively appeared as KC-like syncytia. Although individual KCs could not catch bacteria flowing within larger vessels, KC-like syncytia were able to capture high numbers of circulating bacteria. Using transcriptomic analysis, we identified CD36 as the key molecule underlying syncytial fusion and reduced susceptibility to infection. CR1g-expressing intravascular macrophage syncytia were also found in human cirrhosis of different etiology.

CONCLUSION: Loss of contact with parenchymal cells in the fibrotic niche leads sinusoid-resident KCs to lose identity and function. Because KC replenishment in rarefied sinusoids would serve little purpose, monocytes follow the formation of collateral vessels that bypass sinusoids, where they form KC-like syncytia that have the capacity to capture bacteria from the bloodstream. Thus, KC maladaptation within an altered fibrotic niche environment is rescued by monocytes forming KC-like syncytia to capture bacteria. These cell structures may play a critical evolutionary role that allows mammals to withstand severe chronic insults in the liver. ■

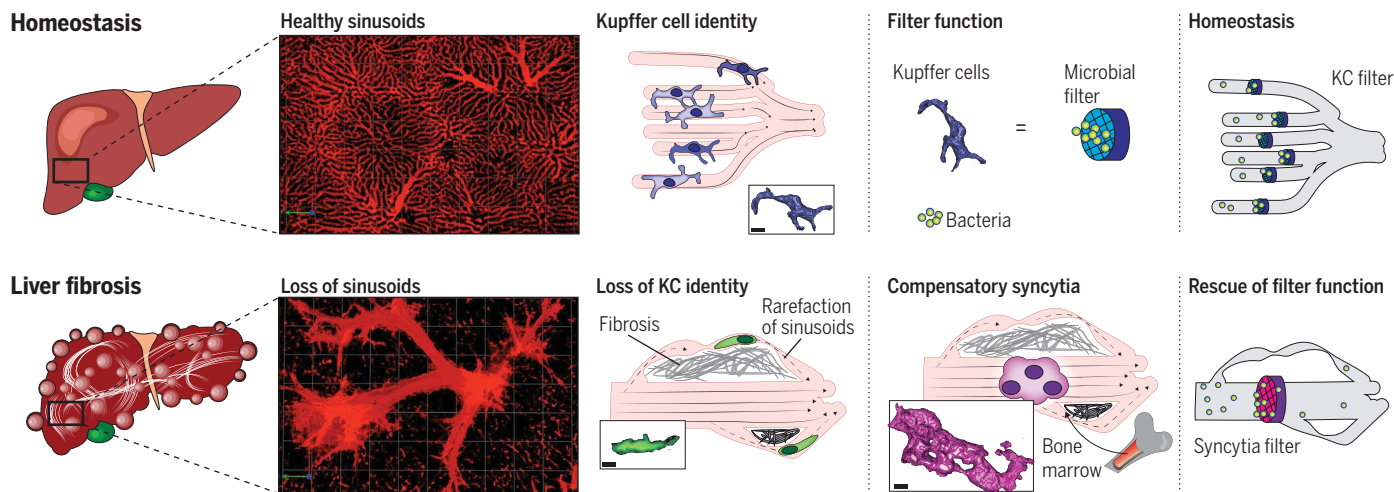
The list of author affiliations is available in the full article online.

*Corresponding author. Email: pkubes@ucalgary.ca

†These authors contributed equally to this work.

Cite this article as M. Peiseler et al., *Science* **381**, eabq5202 (2023). DOI: 10.1126/science.abq5202

S **READ THE FULL ARTICLE AT**
<https://doi.org/10.1126/science.abq5202>



Kupffer cell adaptation in fibrotic liver disease. In healthy livers, KCs reside in sinusoids and rapidly capture blood-borne pathogens. In liver fibrosis, sinusoids are rarefied, leading to redistributed circulation through high-flow collateral vessels. KCs consequently lose their identity and function. Monocytes then seed larger vessels and form KC-like syncytia with the heightened capacity to capture bacteria, providing a rescue adaptation to the fibrosis-induced loss of KCs.

RESEARCH ARTICLE

IMMUNOLOGY

Kupffer cell-like syncytia replenish resident macrophage function in the fibrotic liver

Moritz Peiseler^{1,2,3,4†}, Bruna Araujo David^{1,2†}, Joel Zindel^{1,2,5}, Bas G. J. Surewaard^{1,2}, Woo-Yong Lee^{1,2}, Felix Heymann³, Ysbrand Nusse^{1,2}, Fernanda V. S. Castanheira^{1,2}, Raymond Shim^{1,2}, Adrien Guillot³, Alix Bruneau³, Jawairia Atif⁶, Catia Perciani⁶, Christina Ohland^{1,2}, Priyanka Ganguli Mukherjee⁷, Annika Niehrs⁸, Roland Thuenauer⁸, Marcus Altfeld⁸, Mathias Amrein⁷, Zhaoyuan Liu⁹, Paul M. K. Gordon¹⁰, Kathy McCoy^{1,2,11}, Justin Deniset^{1,2,12,13}, Sonya MacParland⁶, Florent Ginhoux^{14,15}, Frank Tacke³, Paul Kubes^{1,2*}

Kupffer cells (KCs) are localized in liver sinusoids but extend pseudopods to parenchymal cells to maintain their identity and serve as the body's central bacterial filter. Liver cirrhosis drastically alters vascular architecture, but how KCs adapt is unclear. We used a mouse model of liver fibrosis and human tissue to examine immune adaptation. Fibrosis forced KCs to lose contact with parenchymal cells, down-regulating "KC identity," which rendered them incapable of clearing bacteria. Commensals stimulated the recruitment of monocytes through CD44 to a spatially distinct vascular compartment. There, recruited monocytes formed large aggregates of multinucleated cells (syncytia) that expressed phenotypical KC markers and displayed enhanced bacterial capture ability. Syncytia formed via CD36 and were observed in human cirrhosis as a possible antimicrobial defense that evolved with fibrosis.

Positioned at the confluence of the intestinal vasculature and systemic circulation, the liver acts as a major filter of disseminated blood-borne pathogens (1). Liver sinusoids are microanatomical filtration units designed for the optimal surveillance of passing blood (2). Strategically located within these sinusoids is a population of resident macrophages called Kupffer cells (KCs), which represent the most abundant population of tissue macrophages in the human body (3). KCs are characterized by their ramified structures, sessile nature relative to other patrolling immune cells, and primarily

intravascular location (Fig. 1A, fig. S1A, and movie S1). At the same time, their long protrusions interact with liver parenchymal cells (Fig. 1, A and B) including hepatic stellate cells (HSCs), liver sinusoidal endothelial cells (LSECs), and hepatocytes, together forming the KC niche. The interaction between parenchymal cells and KCs is critical for KC function, as parenchymal cells supply important signals that maintain KC identity (4). This niche is optimized for immune surveillance, as blood-borne pathogens are instantaneously captured by KCs (Fig. 1C and movie S2).

Intravital imaging reveals progressive vascular remodeling in liver fibrosis

In order for KCs to capture blood-borne bacteria, sinusoids must be sufficiently narrow so that KCs occupy large amounts of the sinusoidal lumen without restricting blood flow through these channels (Fig. 1C). In chronic liver diseases with fibrosis, architectural changes—regardless of underlying etiology—occur, including the deposition of a basement membrane around sinusoids (capillarization), defenestrated sinusoids, and the development of intrahepatic and extrahepatic shunts and collaterals to accommodate blood flow (5–7). Using intravital microscopy (IVM), we imaged numerous mouse models of liver disease. We found that the carbon tetrachloride (CCl_4) toxicity model produced the most pronounced fibrosis and vascular changes like those seen in human disease, allowing us to study KC immunodynamics in a bona fide fibrotic niche (Fig. 2A). IVM revealed profound parenchymal changes that included narrowing of liver si-

nusoids and dilation of larger venules (Fig. 2A and fig. S1, B and C). Imaging of blood flow revealed the homogeneous perfusion of sinusoids in control livers (fig. S1D and movie S3), whereas livers of CCl_4 -treated mice at 8 weeks showed large collateral vessels and dilated venules with poor or absent perfusion of sinusoids (fig. S1D and movie S3), which are characteristic of human cirrhosis (8–10).

Tracking labeled red blood cells (RBCs) allowed us to quantify hepatic blood flow (Fig. 2, B to D). In control mice, homogeneous sinusoidal blood had a mean flow rate of 52 $\mu\text{m}/\text{s}$, whereas flow in the constricted sinusoids of fibrotic mice was lower (mean flow: 17 $\mu\text{m}/\text{s}$) and often completely occluded (Fig. 2, B and C). In venules, mean flow in control mice was $\sim 200 \mu\text{m}/\text{s}$, whereas mean flow through the collateral vessels of fibrotic mice was 350 $\mu\text{m}/\text{s}$ (Fig. 2, B and D). The flow was often turbulent and not laminar (i.e., RBCs no longer traveled in straight lines) (Fig. 2D). The drastic increase of collateral vessels due to loss of patent capillaries is consistent with a threefold increase in venular cells (11). Furthermore, single-cell sequencing previously revealed that *ACKR1*, a venular endothelium signature gene, is highly enriched in human cirrhosis (12).

Fibrotic remodeling of the Kupffer cell niche

Second-harmonic generation revealed robust collagen deposition around the sinusoids of CCl_4 -treated mice but not sham-treated mice (Fig. 2A), which was not easily seen by conventional histology (fig. S1, E and F). KCs in healthy mice were found exclusively in hepatic sinusoids and projected numerous pseudopods into the space of Disse (Fig. 2, E and F). By contrast, after 8 weeks, CCl_4 -treated mice showed increased fibrosis and sinusoids of reduced diameter harboring macrophages with elongated shapes and significantly fewer pseudopods (Fig. 2, E and F). Patients with liver cirrhosis (stage F4 fibrosis) similarly presented with KCs that had lower average cell size and elongated shape compared with healthy individuals (Fig. 2, G and H, and fig. S1G). Furthermore, IVM of *Lrat^{cre} × Rosa26^{AdTomato}* HSC reporter mice (13) uncovered close contacts between KCs and HSCs in control mice (Fig. 1B and fig. S1H). Colocalization analysis confirmed the intricate anatomical interconnections between KCs and HSCs under homeostatic conditions (Fig. 2I and fig. SII). By contrast, most KCs in the sinusoids of CCl_4 -treated mice were detached from HSCs (Fig. 2I and fig. S1H), as HSCs relocated away from sinusoids and surrounded the large collaterals (fig. S1H), further altering the KC niche.

Macrophages in fibrotic sinusoids are functionally impaired

To investigate the bacterial capture of KCs in sinusoids, we induced bacteremia by intravenous

¹Department of Physiology and Pharmacology, University of Calgary, Calgary, Alberta, Canada. ²Snyder Institute for Chronic Diseases, Cumming School of Medicine, University of Calgary, Calgary, Alberta, Canada. ³Department of Hepatology and Gastroenterology, Charité Universitätsmedizin Berlin, Campus Virchow Klinikum and Campus Charité Mitte, Berlin, Germany. ⁴Berlin Institute of Health (BIH), Berlin, Germany. ⁵Department of Visceral Surgery and Medicine, Department for BioMedical Research (DBMR), University of Bern, Bern, Switzerland.

⁶Ajmera Transplant Centre, Toronto General Research Institute, University Health Network, Toronto, Ontario, Canada.

⁷Department of Cell Biology and Anatomy, University of Calgary, Calgary, Alberta, Canada. ⁸Leibniz Institute of Virology (LIV), Hamburg, Germany. ⁹Shanghai Institute of Immunology, Department of Immunology and Microbiology, Shanghai Jiao Tong University School of Medicine, Shanghai, China. ¹⁰Centre for Health Genomics and Informatics, University of Calgary, Calgary, Alberta, Canada. ¹¹Department of Microbiology, Immunology and Infectious Diseases, Cumming School of Medicine, University of Calgary, Calgary, Alberta, Canada. ¹²Department of Cardiac Sciences, University of Calgary, Calgary, Alberta, Canada. ¹³Libin Cardiovascular Institute, Cumming School of Medicine, University of Calgary, Calgary, Alberta, Canada. ¹⁴Singapore Immunology Network (SIgN), Agency for Science, Technology and Research (A*STAR), Singapore, Singapore. ¹⁵Gustave Roussy Cancer Campus, INSERM U1015, Villejuif, France.

*Corresponding author. Email: pkubes@ucalgary.ca
†These authors contributed equally to this work.

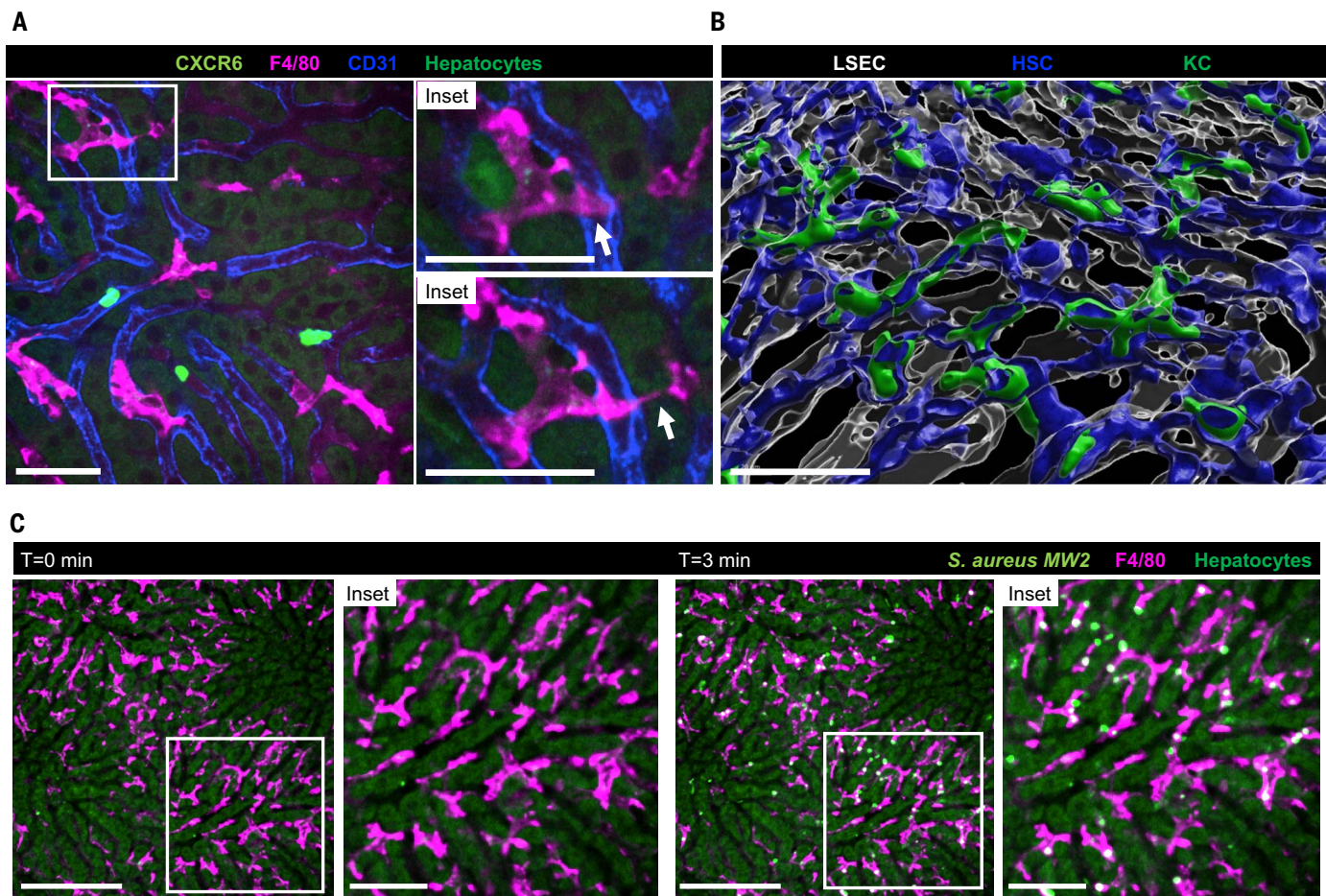


Fig. 1. Immune surveillance by Kupffer cells. (A) Representative IVM image of KCs (magenta) scanning the blood stream with their protrusions. Hepatocytes (dull green), LSECs (blue), and patrolling CXCR6-expressing cells (bright green) are depicted. (Inset) Time-lapse image of a KC sending a protrusion laterally touching another KC (arrow). Scale bars: 50 μ m. (B) Representative 3D surface rendering of the KC niche

showing KCs (green), hepatic stellate cells (blue), and endothelial cells (white). Scale bar: 100 μ m. (C) Representative IVM image of staphylococcal capture (MW2-GFP in bright green) by KCs labeled with F4/80 (magenta) and hepatocytes (dull green) in baseline mice before (left) and 3 min after injection of bacteria showing instant capture of bacteria. Scale bars: 150 μ m and 50 μ m (insets).

injection of a clinically important methicillin-resistant *Staphylococcus aureus* (MRSA) strain expressing a fluorescent reporter (*S. aureus* MW2). In control mice, the vast majority of injected *S. aureus* MW2 were rapidly captured by KCs in the liver sinusoids (Fig. 2J, fig. S1J, and movie S4). By contrast, bacterial capture in the sinusoids of fibrotic mice was reduced (Fig. 2J, fig. S1J, and movie S4). The bacterial burden in the blood and spleens of CCl₄-treated mice was also higher than in controls (Fig. 2K). Moreover, the frequency of F4/80⁺ macrophages in sinusoids that had captured bacteria decreased in fibrosis (Fig. 2L).

Given that KCs also kill the captured staphylococci (14), we next performed intravital imaging of the phagocytic processing capacity of sinusoidal KCs in control and CCl₄-treated mice (15). In control mice, the vast majority of captured bioparticles were rapidly acidified (>95%) (Fig. 2M and movie S5), whereas in CCl₄-treated mice, bioparticle acidification was delayed over the first hour (Fig. 2M and

movie S5), suggesting the loss of KC antimicrobial capacity.

Macrophages in fibrotic sinusoids lose Kupffer cell identity

The morphological and functional changes in the KC compartment in fibrotic sinusoids prompted us to investigate phenotypical adaptation. We focused on two key molecules—complement receptor of the immunoglobulin superfamily [CRIg, also referred to as V-set immunoglobulin-domain-containing 4 (VSIG4)] and T cell membrane protein 4 (TIM-4)—that give KCs their functional phenotype (16). More than 90% of the F4/80⁺ macrophages in the liver sinusoids of control mice coexpressed TIM-4 and CRIg (Fig. 3, A and B). By contrast, fewer F4/80⁺ macrophages from CCl₄-treated mice expressed TIM-4 and/or CRIg (Fig. 3, A and B). These cells were all located within the sinusoids and, by definition, were KCs. F4/80⁺ cells expressing TIM-4 and/or CRIg showed similar cell volumes compared with KCs in control mice, whereas F4/80⁺ macrophages that did not

express either marker were smaller (fig. S2A). All macrophage subsets in fibrotic sinusoids showed similar reductions in contact with HSCs compared with KCs from control sinusoids (fig. S2B).

Using multiparametric flow cytometry and dimensionality reduction with t-distributed stochastic neighbor embedding (tSNE) to cluster hepatic macrophages (fig. S2C), we found that most KCs in control mice expressed high levels of the known KC identity markers C-type lectin like receptor 2 (CLEC2), C-type lectin domain family 4 member F (CLEC4F), CRIg, and TIM-4 (Fig. 3C). By contrast, KCs in mice treated with CCl₄ for 8 weeks consistently had lower levels of all four molecules (Fig. 3C).

CRIg identifies a macrophage subset in fibrotic liver sinusoids with preserved bacterial capture phenotype

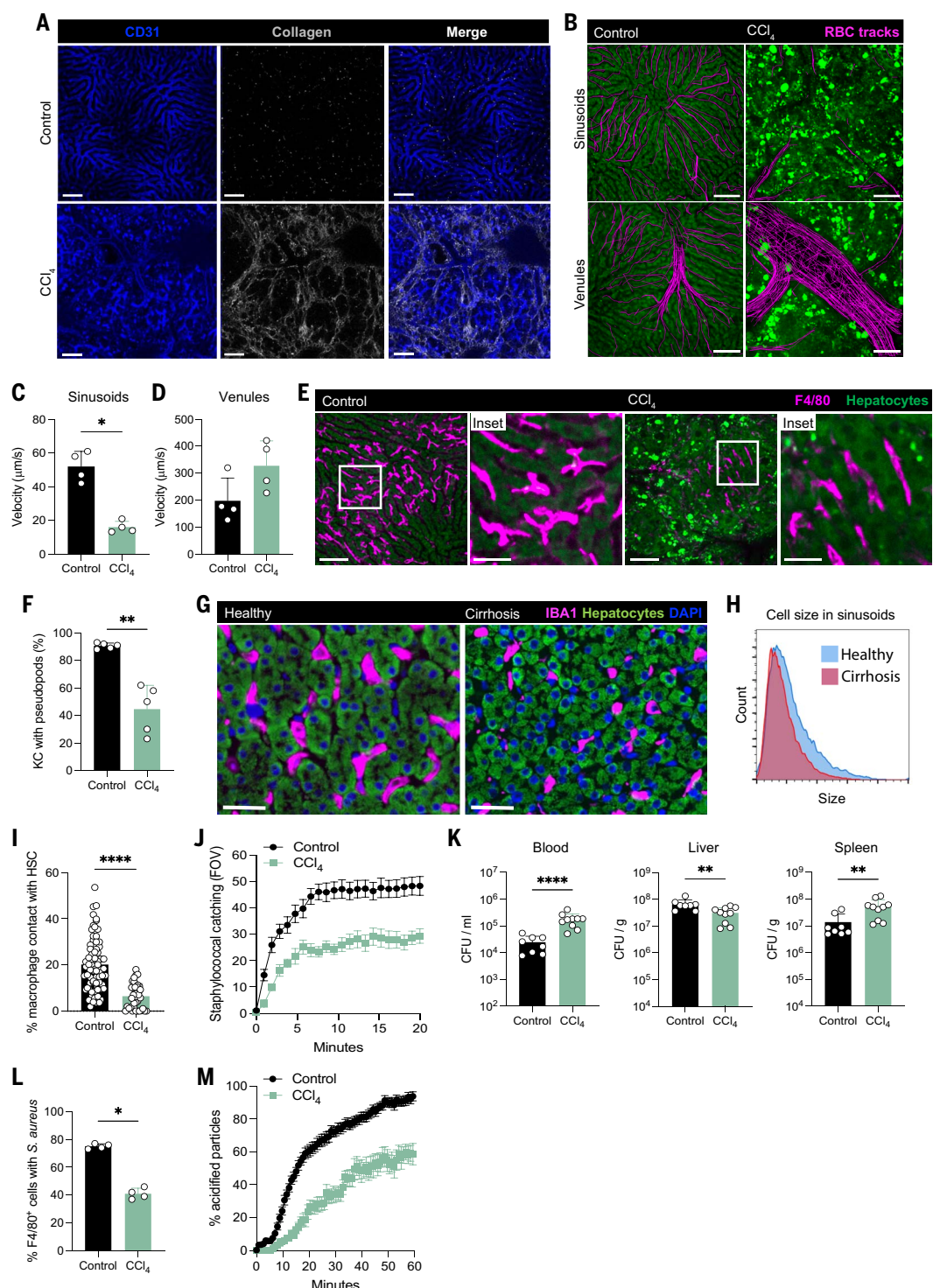
CRIg (VSIG4) is a complement receptor that is critical for KC-mediated bacterial capture (17, 18). Indeed, in both control and CCl₄-treated mice, F4/80⁺CRIg⁺ and F4/80⁺CRIg⁺TIM-4⁺

Fig. 2. Liver fibrosis alters the Kupffer cell niche resulting in a loss of function. (A) Representative multiphoton IVM stitched images of control and fibrotic liver, depicting CD31 (blue) and second-harmonic generation (SHG, white). Scale bars: 200 μ m. (B) Representative IVM images of sinusoids and venules in control and CCl₄-treated mice. RBC tracks visualized (magenta) next to hepatocytes (dull green). Scale bars: 75 μ m. (C and D) Mean velocity of RBC in sinusoids and venules ($n = 4$ per group, $N = 3$). (E) Representative IVM image of KC morphology. KCs (magenta), hepatocytes (dull green), and liver autofluorescence (bright green) Scale bars: 100 μ m and 25 μ m (insets). (F) Quantification of KCs with pseudopods in sinusoids ($n = 5$ per group, $N = 3$). (G) Representative morphology of IBA1⁺ cells (magenta) in human liver cirrhosis. Nuclei (blue) and hepatocytes (green) are depicted. Scale bars: 50 μ m. (H) Individual cell area of IBA1⁺ cells located in the sinusoids of a healthy (blue) and cirrhotic liver (red). (I) Percentage of contact between Lrat-expressing HSCs and F4/80⁺ macrophages in sinusoids ($n = 3$ per group, $N = 3$). (J) Quantification of bacterial capture in control and fibrotic mice infected with 5×10^7 CFU S. aureus MW2 from a 20-min video ($n = 3$ or 4 per group, $N = 3$ or 4). (K) Control and CCl₄-treated mice were infected with 5×10^7 CFU S. aureus MW2, and bacterial loads were determined 30 min after infection ($n = 8$ to 10 per group, $N = 3$ or 4). (L) Frequency of F4/80⁺ cells in sinusoids with bacteria. (M) Quantification of acidification of pHrodo S. aureus bioparticles over 60-min video ($n = 6$ per group, $N = 2$). Data represented as individual values with mean \pm SD and as mean \pm SEM in (J) and (M). Mann-Whitney test used for (C), (D), (F), (I), (K), and (L). * $P < 0.05$, ** $P < 0.01$, *** $P < 0.001$, **** $P < 0.0001$.

macrophages captured bacteria, whereas only a small fraction of F4/80⁺CRIG⁺ cells did so (Fig. 3D and movie S6). Furthermore, F4/80⁺CRIG⁺ TIM-4⁺ and F4/80⁺CRIG⁺ TIM-4⁻ cells exhibited a capture efficiency of around 70% (fig. S2D), which was similar to KCs from control mice (Fig. 2L). By contrast, F4/80⁺CRIG⁺ cells demonstrated very low capture efficiency (fig. S2D).

Ontogeny of hepatic macrophages in liver sinusoids

Recent single-cell studies in models of fatty liver disease suggest that KCs are replaced by recruited monocyte-derived cells on the basis of transcriptomic changes (19–21). To study the ontogeny of sinusoidal KCs, we used *Ms4a3cre* × *Rosa*^{tdTomato} monocyte fate-mapping mice (22), whose bone marrow (BM)-derived precursors, but not res-



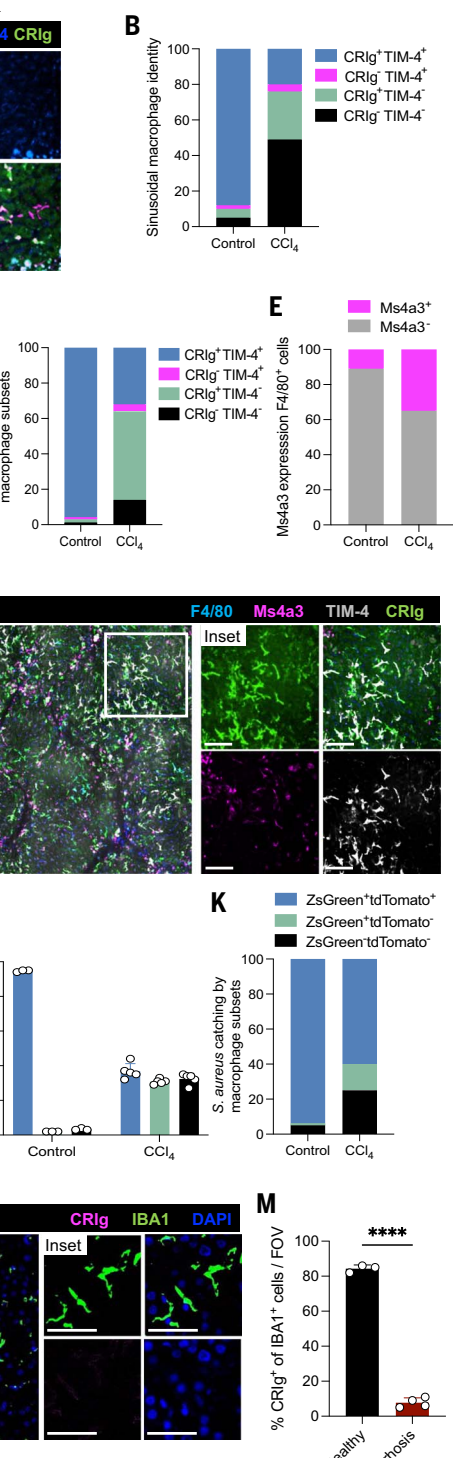
ident fetal liver-derived macrophages, fluoresce. Under homeostatic conditions, 2 to 10% of BM-derived monocytes contributed to the pool of liver macrophages (Fig. 3, E and F, and fig. S2E). After 8 weeks of CCl₄ treatment, ~30% of macrophages in sinusoids were derived from BM-derived monocytes and 70% were fetal liver-derived KCs (Fig. 3, E and F, and fig. S2E). The labeling efficiency of Ms4a3

Fig. 3. Liver fibrosis leads to loss of Kupffer cell identity. (A) Representative IVM images of KC markers F4/80 (magenta), CR Ig (green), and TIM-4 (blue) in control and CCl₄-treated mice. Scale bars: 75 μ m. (B) Quantification of (A) as a percentage of all F4/80⁺ cells in sinusoids ($n = 4$ per group, $N = 3$). (C) tSNE representation showing expression of the key KC markers of CLEC2, TIM-4, CR Ig, and CLEC4F in hepatic macrophages. Cells were pre-gated as live singlet CD45⁺CD19⁻SiglecF⁺F4/80⁺CD11b^{lo}. (D) Distribution of *S. aureus* uptake by different liver macrophages by IVM in sinusoids ($n = 4$ per group, $N = 3$ or 4). (E) Proportion of Ms4a3⁺F4/80⁺ cells in sinusoids in healthy and fibrotic mice ($n = 3$ or 4 per group, $N = 2$). (F) Representative IVM images of Ms4a3⁺ cells (magenta) in control and fibrotic mice in combination with CR Ig (green), TIM-4 (gray), and F4/80 (blue). Scale bars: 250 μ m and 100 μ m (insets). (G and H) BM-derived (Ms4a3⁺) and embryonic (Ms4a3⁻) hepatic macrophage expression of different KC markers and subsets stratified by Ms4a3 expression assessed by IVM in fibrotic mice ($n = 4$ per group, $N = 2$ or 3). (I) Quantification of CD45.1 and CD45.2 expression by sinusoidal macrophages in control and CCl₄-treated parabiotic mice ($n = 4$ or 5 per group, $N = 4$). (J) Quantification of

tdTomato, ZsGreen, and F4/80 expression by sinusoidal macrophages assessed by IVM ($n = 3$ to 5 per group, $N = 3$). (K) Distribution of caught *S. aureus* in the different macrophage subsets in control and CCl₄-treated mice ($n = 3$ per group, $N = 2$). (L) Representative immunofluorescence images showing KCs in healthy (left) and cirrhotic (right) human livers. Depicted are IBA1⁺ cells (green) with CR Ig (magenta) and nuclei (blue). Scale bars: 120 μ m and 50 μ m (insets). (M) Frequency of CR Ig expression by IBA1⁺ macrophages in healthy and cirrhotic livers (3 or 4 samples per group). Data represented as individual values with mean \pm SD. Mann-Whitney test was used for (I), (J), and (M). ***P < 0.0001.

(membrane-spanning 4-domains subfamily A member 3) in peripheral blood was consistently around 95% in both control and fibrotic mice (fig. S2, F and G), as previously reported (22).

Stratifying BM-derived Ms4a3⁺F4/80⁺ and embryonic Ms4a3⁻F4/80⁺ cells into those expressing CR Ig and TIM-4 revealed similar proportions of these markers in both embryonic and BM-derived cells, suggesting that the KCs were de-



differentiating during fibrosis (Fig. 3G). In addition, F4/80⁺CR Ig⁺TIM-4⁺ cells had the lowest proportion of Ms4a3, but F4/80⁺CR Ig⁺TIM-4⁻ and F4/80⁺CR Ig⁻TIM-4⁻ cells had a <50% rate of replacement by monocytes (Fig. 3H). Harvesting

all macrophages from liver, not just KCs, revealed that 40 to 50% of F4/80⁺ hepatic macrophages were Ms4a3⁻ (fig. S2H), including monocyte recruitment to other liver compartments (subcapsular, etc.). KCs from CCl₄-treated mice had similar levels of CRIG and TIM-4 expression in BM and embryonic macrophages (fig. S2, I and J). We concluded that the lack of niche signals drove tissue-resident and monocyte-derived macrophages asymptotically toward a similar fibrosis-associated phenotype. Parabiosis of CCl₄-treated mice (fig. S2K) and imaging revealed that most F4/80⁺ cells in liver sinusoids (KCs) were host-derived macrophages, and partner-derived macrophages accounted for <10% at 8 weeks of disease (Fig. 3I and fig. S2L). Moreover, chimerism of host- and partner-derived KCs (F4/80^{hi}CD11b^{lo} cells) was between 5 and 10% (fig. S2, M and N). Similarly, the proportion of KCs expressing CRIG was similar in host- and partner-derived KCs (fig. S2O).

We next used the *Clec4f*^{cre-tdTomato} × *Rosa26*^{ZsGreen} mouse, a dual reporter for both active expression (tdTomato) and previous expression (ZsGreen) of CLEC4F. More than 95% of F4/80⁺ cells in sinusoids coexpressed tdTomato and ZsGreen, indicating an active KC phenotype (Fig. 3J and fig. S3A). In CCl₄-treated mice, we found three populations of F4/80⁺ cells in the sinusoids: tdTomato⁺ZsGreen⁺ KCs, tdTomato⁺ZsGreen⁺ former KCs (exKC), and F4/80⁺ cells with no history of CLEC4F expression (Fig. 3J and fig. S3A). This suggested that some KCs had down-regulated CLEC4F in addition to the KC markers CRIG and/or TIM-4 (fig. S3B).

Principal components analysis (PCA) of sorted F4/80^{hi}CD11b^{lo}Ms4a3⁻ embryonic KCs from both control and CCl₄-treated mice revealed distinct gene expression profiles (fig. S3C). Out of 22,109 genes, embryonic liver macrophages from fibrotic livers differentially expressed 4298 genes compared with healthy controls, including down-regulation of *Clec4f*, *Vsig4* (CRIG), and *Timd4* (fig. S3D). Recent studies have identified that key transcription factors control KC identity, (23–25) and are expressed as a result of direct contact with parenchymal cells (4). LXRA (*Nrlh3*) is dependent on contact with HSCs and LSECs, whereas ID3 requires hepatocytes (4). In agreement with this model, KCs down-regulated *Nrlh3* as they lost contact with HSCs (fig. S3D). By contrast, *Id3* levels did not change, possibly because hepatocyte-derived ID3-activating and/or soluble molecules could still reach the KCs in the context of fibrosis.

We challenged *Ms4a3*^{cre} × *Rosa*^{tdTomato} mice with *S. aureus* MW2 and performed flow cytometric analyses 20 min later (fig. S3, F to H). Although the frequency of F4/80⁺ cells containing *S. aureus* MW2 was reduced in CCl₄-treated mice, there were no detectable differences between Ms4a3⁺ and Ms4a3⁻ cells (fig. S3E). Furthermore, CRIG⁺TIM-4⁺ cells (Ms4a3⁺ and

Ms4a3⁻) caught the most bacteria, irrespective of ontogeny (fig. S3, F and G). In *Clec4f*^{cre-tdTomato} × *Rosa26*^{ZsGreen} mice treated with CCl₄, bacterial uptake was superior in ZsGreen⁺tdTomato⁺F4/80⁺ KCs (Fig. 3K and fig. S3H), demonstrating that a KC phenotype was required for proficient bacterial capture even in fibrosis. Loss of KC identity could also be seen in liver biopsies of patients with liver cirrhosis. There was a loss of CRIG in IBA1⁺ human liver macrophages in sinusoids compared with healthy control samples (Fig. 3, L and M).

Physical factors such as reduced blood flow also affected the capture ability of the KCs. Reducing portal flow by 70% in healthy mice (fig. S3I) reduced bacterial capture (fig. S3J). Bacteria still circulated through the sinusoids but were not caught, as evidenced by a sharp rise in free-flowing bacteria during reduced flow (fig. S3J). Thus, a certain level of shear was required for adequate bacterial capture, which was lost in fibrotic sinusoids.

Kupffer cell-like macrophage clusters form with enhanced bacterial capture proficiency

Despite significantly impaired KC capture and killing ability in the sinusoids of fibrotic livers, the majority of bacteria were trapped by this organ (Fig. 2K). Furthermore, there were only small differences in overall survival after infection with 5 × 10⁷ colony-forming units (CFU) of *S. aureus* MW2. Over 7 days, 100% of control mice survived, whereas 75 to 80% survived in the CCl₄-treated group (Fig. 4A). By contrast, depletion of macrophages in control mice using clodronate liposomes (fig. S4A) or genetically depleting KCs (*Clec4f*^{cre-tdTomato} × *Rosa26*^{IDTR} mouse) (Fig. 4B and fig. S4B) induced 100 and 80% mortality, respectively, within 48 hours after *S. aureus* MW2 infection. In healthy mice, KCs were localized exclusively in liver sinusoids and not larger venules (fig. S4C). By contrast, fibrotic mice showed progressive accumulation of F4/80⁺ cells in larger venules (fig. S4C). By 8 weeks, CCl₄-treated mice formed large aggregates of F4/80⁺ macrophages that occupied most of the width of large collateral vessel lumina (Fig. 4C). Collateral vessels appeared to have an abundance of these clusters in larger stitched images, especially at bifurcations, with the occasional individual F4/80⁺ macrophage observed within these larger vessels (Fig. 4C).

Upon challenge with intravenous *S. aureus* MW2, these macrophage aggregates were extraordinarily efficient at capturing bacteria out of the bloodstream of the collaterals under high shear conditions (Movie 1 and movie S7). In control mice, infection with 5 × 10⁷ *S. aureus* MW2 resulted in an evenly distributed uptake of bacteria by KCs in the liver sinusoids, with 1 to 2 staphylococci captured per KC (movies S2 and S7). By contrast, in fibrotic livers, individual clusters captured large numbers of bacteria (Movie 1, fig. S4D, and movie S7), in some instances exceeding 20 to 30 staphylococci per cluster. Moreover, most large clusters expressed high levels of CRIG (Fig. 4D and movie S7). CRIG^{-/-} mice also formed macrophage aggregates after 8 weeks of CCl₄ treatment but could not capture bacteria (Fig. 4G and fig. S4E) and had increased bacteremia and reduced CFU in the liver after intravenous administration of *S. aureus* MW2 compared with wild-type (WT) CCl₄-treated mice (Fig. 4H). These clusters also rapidly acidified pHrodo *S. aureus* bioparticles (Fig. 4I and fig. S4F) at kinetics similar to KCs in control mice. This very efficient clearance of bacteria from high-flow vessels by macrophage aggregates was drastically reduced by mechanical reduction of hepatic flow and quickly restored after blood flow was normalized (Fig. 4J). Thus, the emergence of CRIG-expressing macrophage clusters shifted the capture capacity of the liver from sinusoids to collateral venules in fibrotic livers.

M multinucleated macrophage syncytia are found in human liver diseases

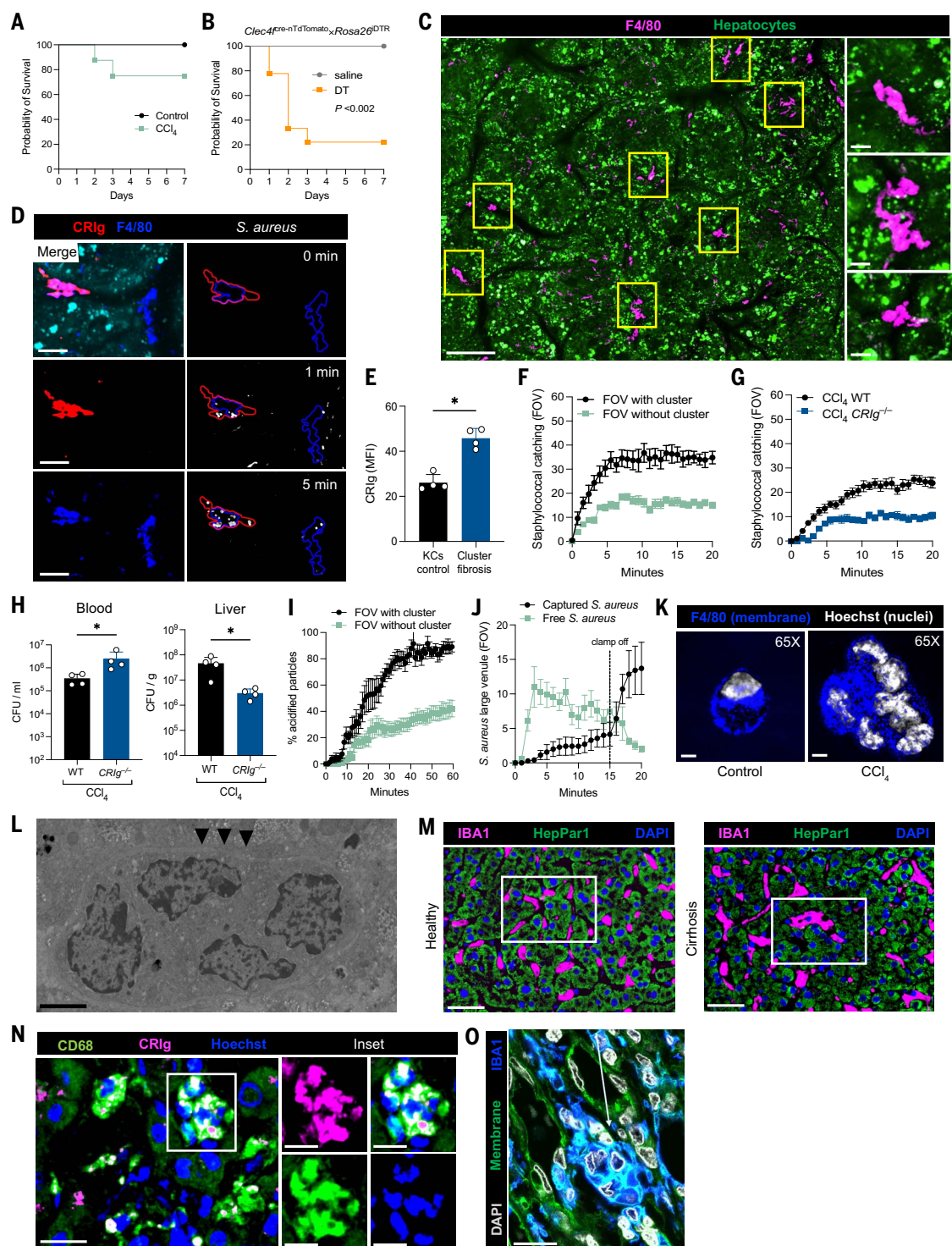
High-resolution microscopy (Fig. 4K) and transmission electron microscopy (TEM) (Fig. 4L) identified multinucleated giant macrophages in mouse fibrotic livers, indicating that in some instances these cells fused into giant cells. However, our imaging unveiled a spectrum of macrophage phenotypes ranging from clusters of individual cells up to and including multinucleated giant cells. Therefore, we called these structures “Kupffer cell-like syncytia.”

In a multicenter approach with three liver transplant centers, we systematically assessed human cirrhotic liver tissue. We found numerous clusters of CD68⁺ multinucleated giant cells in patients with liver cirrhosis from different etiologies, including chronic viral hepatitis, alcoholic liver disease, nonalcoholic fatty liver disease, and cholestatic liver diseases (Fig. 4, M to O, and fig. S4, G and H). IBA1 staining, which identifies all macrophages (26), revealed the presence of intravascularly located large macrophages with multiple nuclei (Fig. 4, M to O, and fig. S4H). These KC-like syncytia were also positive for CRIG (Fig. 4N).

Kupffer cell-like syncytia are of bone marrow origin

With their intravascular location, high surface expression of CRIG, and superior bacterial capture capacity, syncytia resembled bona fide KCs. Indeed, IVM revealed the KC-like syncytia expressed TIM-4 and CLEC4F (Fig. 5, A to D, and fig. S5, A and B). Furthermore, the KC-like syncytia were in close proximity to the HSCs that had relocated around the large collaterals, potentially inducing the KC molecules (fig. S1H). Despite their KC-like phenotype, ~90% of the syncytia expressed Ms4a3 (Fig. 5, C and D, and fig. S5B), consistent with their primarily monocyte-derived origin. Liver injury leads

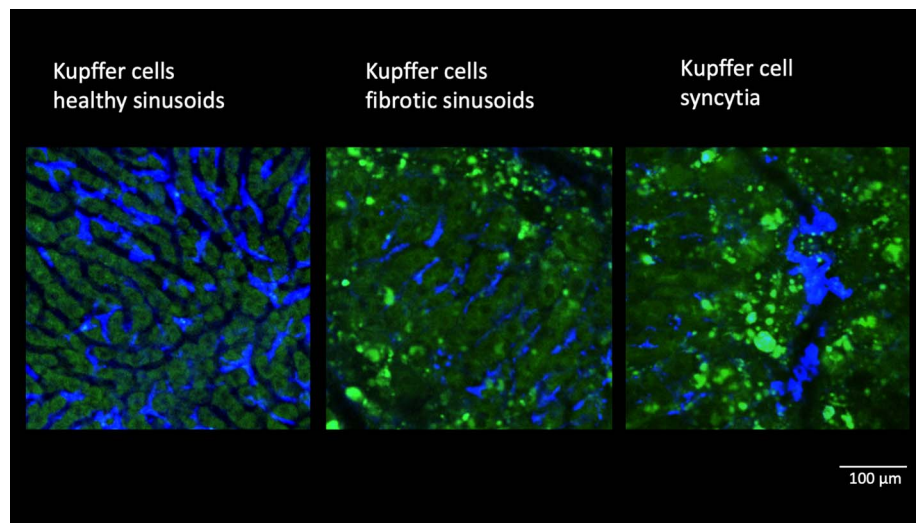
Fig. 4. Multinucleated syncytia emerge in fibrosis with enhanced Kupffer cell features. (A and B) Survival of mice infected with 5×10^7 CFU *S. aureus* MW2. (A) Control and CCl₄-treated mice ($n = 8$ per group, $N = 2$) and (B) *Clec4f*^{cre-nTdT}Tomato^xRosa26^{DTR} mice 24 hours after application of diphtheria toxin or saline ($n = 7$ to 9 per group, $N = 2$). (C) Representative stitched IVM showing clusters of F4/80⁺ macrophages (magenta) in large vessels (inset), hepatocytes (dull green), and tissue auto-fluorescence (bright green). Scale bars: 250 μ m and 20 μ m (insets). (D) Macrophage cluster (blue) at vascular bifurcation expressing high levels of CR Ig (red). Scale bars: 50 μ m. (E) CR Ig mean fluorescent intensity of KCs in control mice and macrophage clusters in fibrotic mice ($n = 4$ per group, $N = 2$). (F) Staphylococcal capture in CCl₄-treated mice comparing FOV with and without clusters in large vessels ($n = 3$ or 4 per group, $N = 4$). (G) Quantification of staphylococcal capture in WT or CR Ig^{-/-} fibrotic mice ($n = 4$ per group, $N = 2$). (H) Bacterial burden in WT and CR Ig^{-/-} fibrotic mice infected with 5×10^7 CFU *S. aureus* ($n = 4$ per group, $N = 2$). (I) Kinetics of particle acidification by macrophage clusters ($n = 3$ per group, $N = 2$). (J) Quantification of staphylococcal capture in fibrotic venules with the portal vein clamped and removed after 15 min. (K) Ex vivo isolated macrophages from control and fibrotic livers. F4/80 (blue) and Hoechst dye (white) indicate plasma membrane and nuclei, respectively. Scale bars: 10 μ m. (L) Electron microscopy image of multinucleated giant cell in a CCl₄-treated mouse. Arrows indicate the cell wall. Scale bar: 10 μ m. (M) Representative immunofluorescent staining with IBA1 (macrophages, magenta), HepPar1 (hepatocytes, green), and DAPI (nuclei, blue) showing multinucleated intravascular macrophages in cirrhosis. Scale bars: 50 μ m. (N) Representative immunofluorescence image of multinucleated macrophages in cirrhosis expressing CD68 (green), CR Ig (magenta), and nuclei (blue) shown. Scale bars: 50 μ m and 25 μ m (insets). (O) Multinucleated syncytia in liver cirrhosis showing IBA1 (blue), DAPI (white), and sodium potassium ATPase (green) to label cell membrane. Scale bar: 30 μ m. Data represented as individual values with mean \pm SD and as mean \pm SEM in (F), (G), (I), and (J). Mann-Whitney test was used in (E) and (H). Log-rank test was used for (A) and (B). * $P < 0.05$, ** $P < 0.01$.



to prominent recruitment of monocytes (27). IVM revealed extensive recruitment of CX3CR1-expressing monocytes within the larger vessels but not sinusoids at 2 weeks of CCl₄ treatment,

with peak levels at 4 weeks (Fig. 5E and fig. S5C). CX3CR1-expressing monocytes were located in large vessels and started to express F4/80 (fig. S5C), whereas KCs, which lack *Cx3cr1*

(28), were positioned in the surrounding sinusoids (Fig. 5E). Imaging of parabiotic mice whose circulatory systems were conjoined revealed that the KC-like syncytia comprised both



Movie 1. The KC capture function in health and disease. Part 1: Bacterial capture of injected *S. aureus* (white) in control mice is performed rapidly by KCs in the sinusoids (blue). Part 2: Bacterial capture in fibrotic sinusoids is suboptimal, with fewer bacteria caught (white) by morphologically altered KCs (blue). Part 3: Rescue KC-like syncytia occupy larger venules in fibrotic livers and catch many bacteria. Movie runtime: 15 min. Scale bar: 100 μ m.

host (CD45.2) and partner-derived (CD45.1) cells. Thus, we conclude that circulating monocytes contribute to the formation of KC-like syncytia (fig. S5D).

Monocytes recruited at 4 weeks of CCl₄ treatment but not earlier were the source of KC-like syncytia (Fig. 5, F and G, and fig. S5E), as revealed by tamoxifen-inducible fate mapping using *Cx3cr1*^{YFP-creER} \times *Rosa26*^{TdTomato} mice (29). PKH dye was next administered to mice before induction of CCl₄ for long-term labeling of resident macrophages (30). Sinusoidal KCs but not the syncytia were labeled with PKH after 8 weeks of CCl₄ treatment, suggesting that KCs did not contribute to syncytia (Fig. 5, H and I). Notably, these KC-like syncytia only formed within the fibrotic liver and not in other organs, such as the lungs or spleen (fig. S5, F and G).

The microbiome drives monocyte recruitment and syncytial formation through MyD88 signaling

Bacterial translocation from the gut is a feature of human cirrhosis (31). Mice treated with a cocktail of broad-spectrum antibiotics from birth (Fig. 6A) or germ-free (GF) mice exhibited greatly reduced syncytial formation after CCl₄ treatment (Fig. 6B). Moreover, intravenous administration of *S. aureus* MW2 resulted in reduced bacterial capture by the liver and increased bacterial numbers in blood of antibiotics-treated or GF mice (Fig. 6, C to F). The lack of a microbiome had no significant effect on the development of CCl₄-driven fibrosis, however (fig. S6A). *Myd88*^{-/-} mice treated with CCl₄ also exhibited reduced syncytial formation (Fig. 6G and fig. S6B), impaired bacterial capture, and increased bacteremia (fig. S6C). Thus, the micro-

biome appears to play a crucial part in the formation of KC-like syncytia.

CD44 is critical in the selective recruitment of monocytes to form Kupffer cell-like syncytia

To better understand KC-like syncytial formation, we interrogated a recently published transcriptomic dataset of mononuclear phagocytes in the CCl₄ fibrosis model and human liver cirrhosis (12). Using the same clustering strategy (fig. S6D) and focusing on KC and monocyte gene expression for cell fusion and adhesion molecules listed in the Gene Expression Omnibus (GEO) term “cell-cell fusion” (GO:0140253), *Cd9*, *Cd36*, and *Cd44* were some of the most highly up-regulated genes associated with adhesion and fusion. By contrast, known molecules involved in macrophage fusion (32), including *Dectin-1*, *Il4*, and *Tnfrsf11a* (RANK) were not highly expressed in recruited monocytes or macrophages in the fibrotic liver (fig. S6, E and F).

CD44 is the dominant adhesive mechanism for numerous cell types in the liver (33–36). The large increase in monocytes in the collateral vessels at 4 weeks of CCl₄ treatment was reduced by >80% in *Cd44*^{-/-} mice (Fig. 6, I and J) leading to no KC-like syncytial formation at 8 weeks after CCl₄ treatment (Fig. 6K and fig. S6G). Because CD44 is expressed by endothelial cells as well as monocytes, we next generated BM chimeras and found that only BM-derived CD44 but not parenchymal cell CD44 was required for KC-like syncytial formation after 8 weeks of CCl₄ treatment (Fig. 6L). Bacterial capture was markedly reduced in *Cd44*^{-/-} mice compared with WT mice treated with CCl₄ (Fig. 6M). *Cd44*^{-/-} mice showed increased bacteremia 30 min after infection and one-third the

amount of CFU in fibrotic livers (Fig. 6N). The importance of KC-like syncytia for antimicrobial defense was confirmed in BM chimeras, as mice with KC-like syncytia formation (WT BM \rightarrow *Cd44*^{-/-} mice) showed superior bacterial capture and reduced bacteremia (Fig. 6, O and P). Only 25% of CCl₄-treated WT mice succumbed to infection, whereas all *Cd44*^{-/-} CCl₄-treated mice died by day 4 after infection (Fig. 6Q). By contrast, all vehicle-treated WT and *Cd44*^{-/-} mice survived infection because, in the absence of liver disease, there was presumably no need for syncytia (Fig. 6Q).

The scavenger receptor CD36 functions as a critical fusion molecule for syncytial generation

The fusion and adhesion molecules *Cd9* and *Cd36* were highly expressed on the monocytes infiltrating fibrotic liver (fig. S6, D to F). Anti-*Cd9* blocking antibody had no effect on syncytia in mice treated with CCl₄ (fig. S6H). By contrast, *Cd36*^{-/-} mice failed to form syncytia after CCl₄ administration but still had an abundance of CRIG⁺F4/80⁺ cells in the collateral vessels (Fig. 7A), suggesting that *Cd36*^{-/-} monocytes were recruited but failed to form syncytia and instead presented as dispersed individual macrophages (Fig. 7A). Individual monocytes took up much less volume within the collaterals compared with KC-like syncytia (Fig. 7, B and C). Because CD36 is expressed by other cells, including hepatocytes, we also generated BM chimeras between WT and *Cd36*^{-/-} mice. Only BM-derived CD36 was required for the formation of KC-like syncytia, however (fig. S7, A and B and Fig. 7D).

Next, we tested bacterial capture in *Cd36*^{-/-} fibrotic mice. CCl₄-treated *Cd36*^{-/-} macrophages lacked the ability to capture bacteria in larger vessels (Fig. 7, E and F, and movie S8) despite expressing ample amounts of cell-surface CRIG. BM chimeras with KC-like syncytia (WT \rightarrow *Cd36*^{-/-}) were more efficient at bacterial capture compared with chimeras without syncytia (*Cd36*^{-/-} \rightarrow WT) and had enhanced bacterial clearance of the blood stream (Fig. 7, G and H). In addition, *Cd36*^{-/-} mice showed a nearly four-fold increase in bacteremia and concomitantly reduced bacterial counts in the liver (Fig. 7F). This was consistent with the hypothesis that the formation of syncytia is necessary to capture bacteria in large collateral vessels. In *Cd36*^{-/-} mice that received no CCl₄, there was no observed impairment in *S. aureus* MW2 capture (fig. S7C), and both WT and *Cd36*^{-/-} control mice survived the 7-day observation period after *S. aureus* MW2 infection. By contrast, CCl₄-treated *Cd36*^{-/-} mice exhibited 80% mortality after *S. aureus* MW2 administration compared with 25% mortality in CCl₄-treated WT mice (Fig. 7I).

Discussion

Two hallmark features of chronic liver diseases are profound architectural changes and the

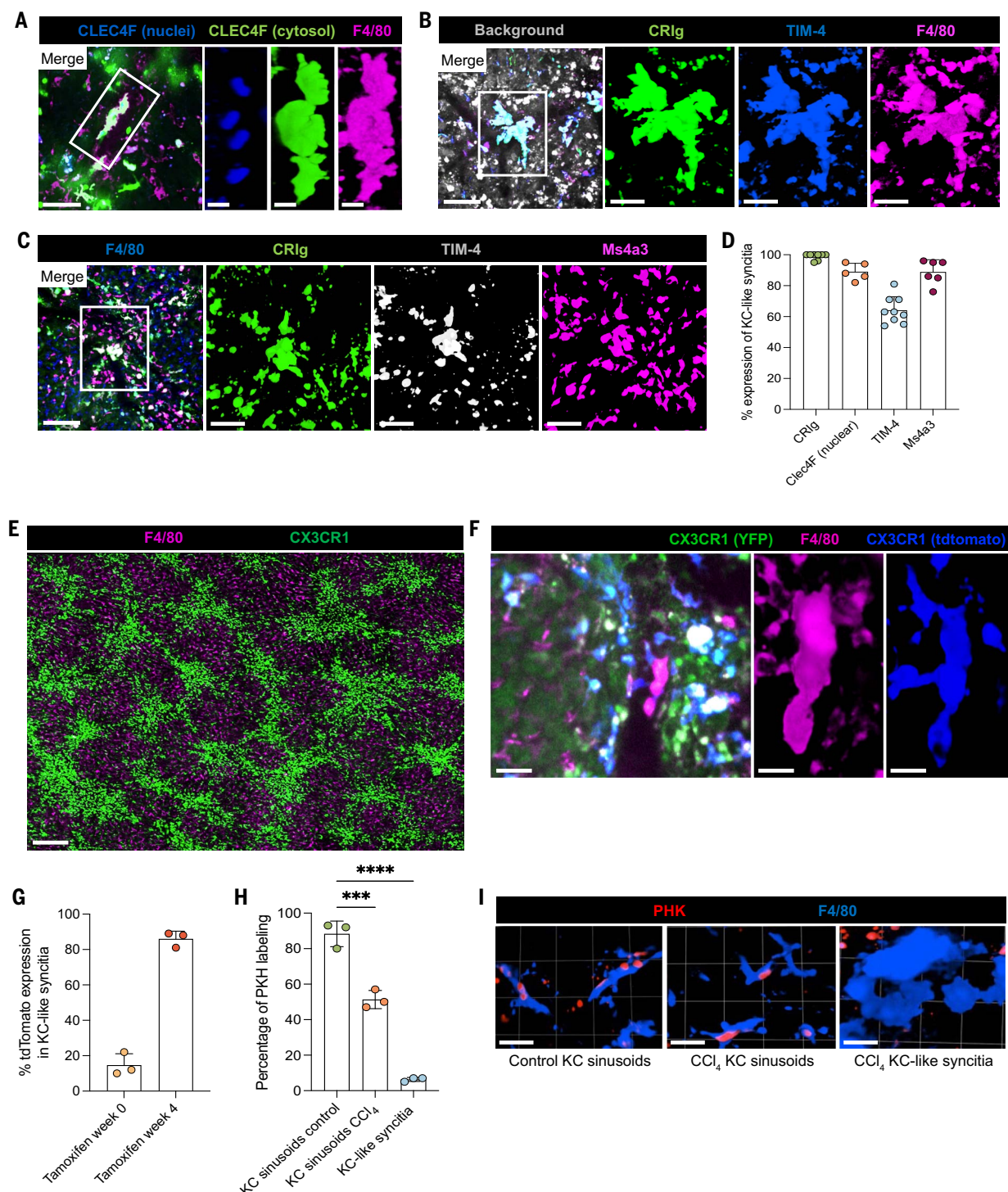
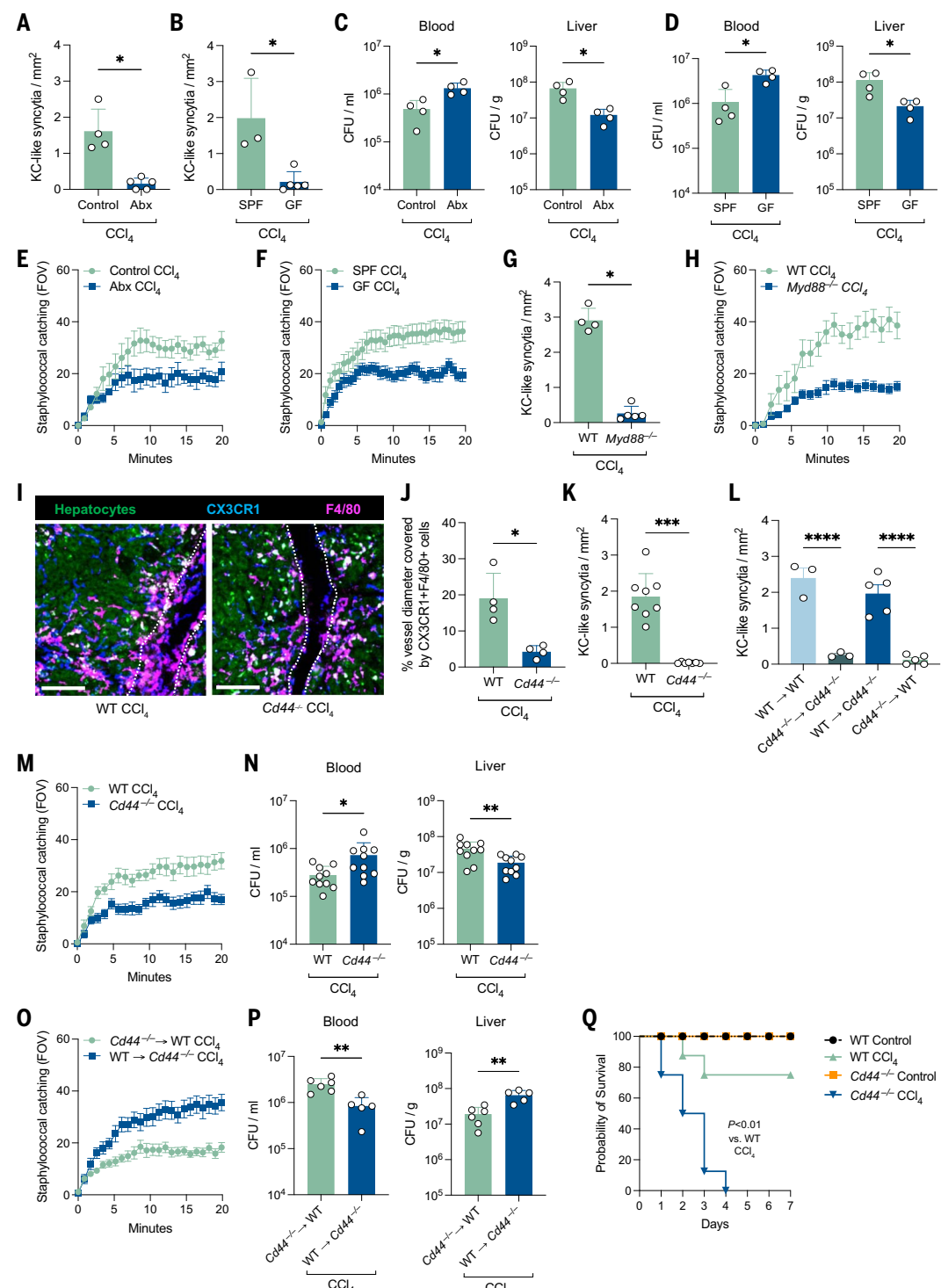


Fig. 5. Syncytia have a Kupffer cell phenotype and are of bone marrow origin. (A) 3D-reconstruction of KC-like syncytia in *Clec4f*^{cre-nTdT-Tomato} × *Rosa26*^{ZsGreen} mice treated with CCl₄. Cytosolic CLEC4F (green) and nuclear CLEC4F (blue) indicate KC phenotype with multiple nuclei together with F4/80 expression (magenta). Scale bars: 100 μm and 20 μm (insets). (B) Representative IVM image of KC-like syncytia labeled with TIM-4 (blue), CRIG (green), and F4/80 (purple). Scale bars: 100 μm and 50 μm (insets). (C) Representative IVM image of *Ms4a3*^{cre} × *Rosa*^{tdTomato} mice treated with CCl₄ showing bone marrow origin of KC-like syncytia with Ms4a3 (magenta), CRIG (green), F4/80 (blue), and TIM-4 (gray). Scale bars: 100 μm and 50 μm (insets). (D) Quantification of KC marker expression and fate mapping of syncytia. (E) Representative stitched IVM image of *Cx3cr1*^{gfp/wt} mouse treated

with CCl₄ (2 weeks) showing accumulation of CX3CR1⁺ cells (bright green) in pericentral and periportal regions and sinusoidal F4/80⁺ KCs (magenta). Scale bar: 500 μm. (F) Representative IVM with 3D reconstruction of KC-like syncytia labeled with F4/80 (magenta) and fate mapping positive (blue, *tdTomato*). Hepatocytes in dull green and CX3CR1-expressing cells in bright green (left panel). Scale bars: 50 μm and 30 μm (insets). (G) Quantification of tamoxifen-inducible fate mapping at weeks 0 and 4 after tamoxifen injection. (H and I) Long-term PHK labeling of KCs before CCl₄ treatment. In control mice and in fibrotic sinusoidal KCs, PHK is detected (red). In KC-like syncytia, PHK is absent ($n = 3$ per group, $N = 2$). Grids: 25 μm. Data represented as individual values with mean ± SD. One-way ANOVA with Tukey's multiple comparisons test was used for (H). *** $P < 0.001$, **** $P < 0.0001$.

Fig. 6. Kupffer cell-like syncytia are recruited through CD44 and commensal microbes. (A and B) Quantification of KC-like syncytia in antibiotics-treated and control fibrotic mice ($n = 4$ or 5 per group, $N = 2$) and in specific pathogen-free (SPF) and germ-free (GF) fibrotic mice ($n = 3$ or 4 per group, $N = 2$). (C and D) Bacterial dissemination in control and antibiotics-treated (Abx) and SPF and GF fibrotic mice infected with 5×10^7 CFU *S. aureus* MW2 ($n = 4$ per group, $N = 2$). (E and F) Quantification of staphylococcal capture in control and antibiotics-treated and SPF and GF fibrotic mice infected with 5×10^7 CFU *S. aureus* MW2 ($n = 4$ per group, $N = 2$). (G) Quantification of KC-like syncytia in WT and *Myd88*^{-/-} mice ($n = 4$ or 5 per group, $N = 2$) treated with CCl₄. (H) Quantification of staphylococcal capture in WT and *Myd88*^{-/-} fibrotic mice ($n = 4$ per group, $N = 2$). (I) Surface area covered by CX3CR1⁺ (blue) and F4/80⁺ (magenta) cells in venules ($n = 4$ or 5 per group) of WT and *Cd44*^{-/-} mice treated with CCl₄ for 4 weeks. Hepatocytes are depicted in dull green. Scale bars: 100 μ m. (J) Quantification of (I). (K and L) Quantification of KC-like syncytia in WT and *Cd44*^{-/-} mice ($n = 7$ or 8 per group, $N = 3$) and WT and *Cd44*^{-/-} bone marrow chimeric mice ($n = 3$ to 5 per group, $N = 2$). (M) Quantification of staphylococcal capture in WT and *Cd44*^{-/-} CCl₄-treated mice ($n = 4$ per group, $N = 2$). (N) Bacterial burden assessed in WT and *Cd44*^{-/-} CCl₄-treated mice ($n = 10$ per group, $N = 3$). (O) Quantification of staphylococcal capture in bone marrow chimeras with WT and *Cd44*^{-/-} bone marrow transplantation ($n = 4$ per group, $N = 2$). (P) Bacterial burden assessed in WT and *Cd44*^{-/-} CCl₄-treated bone marrow chimeras ($n = 5$ or 6 per group, $N = 2$). (Q) Survival analysis of WT and *Cd44*^{-/-} mice treated with corn oil or CCl₄ for 8 weeks and then infected with 5×10^7 CFU *S. aureus* MW2 ($n = 8$ per group). Data represented as individual values with mean \pm SD, data in (E), (F), (H), (M), and (O) are displayed as mean \pm SEM. Mann-Whitney test was used for (A) to (D), (G), (J), (K), (N), and (P). One-way ANOVA with Tukey post hoc test was used in (L). Log-rank test used in (Q). * $P < 0.05$, ** $P < 0.01$, *** $P < 0.001$, **** $P < 0.0001$.



recruitment of monocytes that are thought to augment and replace the pool of KCs found in healthy livers (2, 6, 37). On the basis of imaging and numerous lineage-tracing approaches, we propose that the disappearance of sinusoidal F4/80-expressing macrophages (KCs) is in part due to substantial alteration of their phenotype.

They essentially lose both their liver macrophage identity and their primary function, to capture bacteria within sinusoids. These changes are associated with a substantially altered niche. We also find that monocytes enter the liver and acquire the function of KCs. They do not assume the spatial location of KCs, however,

as fibrotic sinusoids are poorly perfused, allowing for poor bacterial capture. Our model suggests that these monocytes form KC-like syncytia, shifting antimicrobial defense in the liver from the sinusoids to the large collateral vessels that accommodate most of the blood flow traversing the liver. The increased

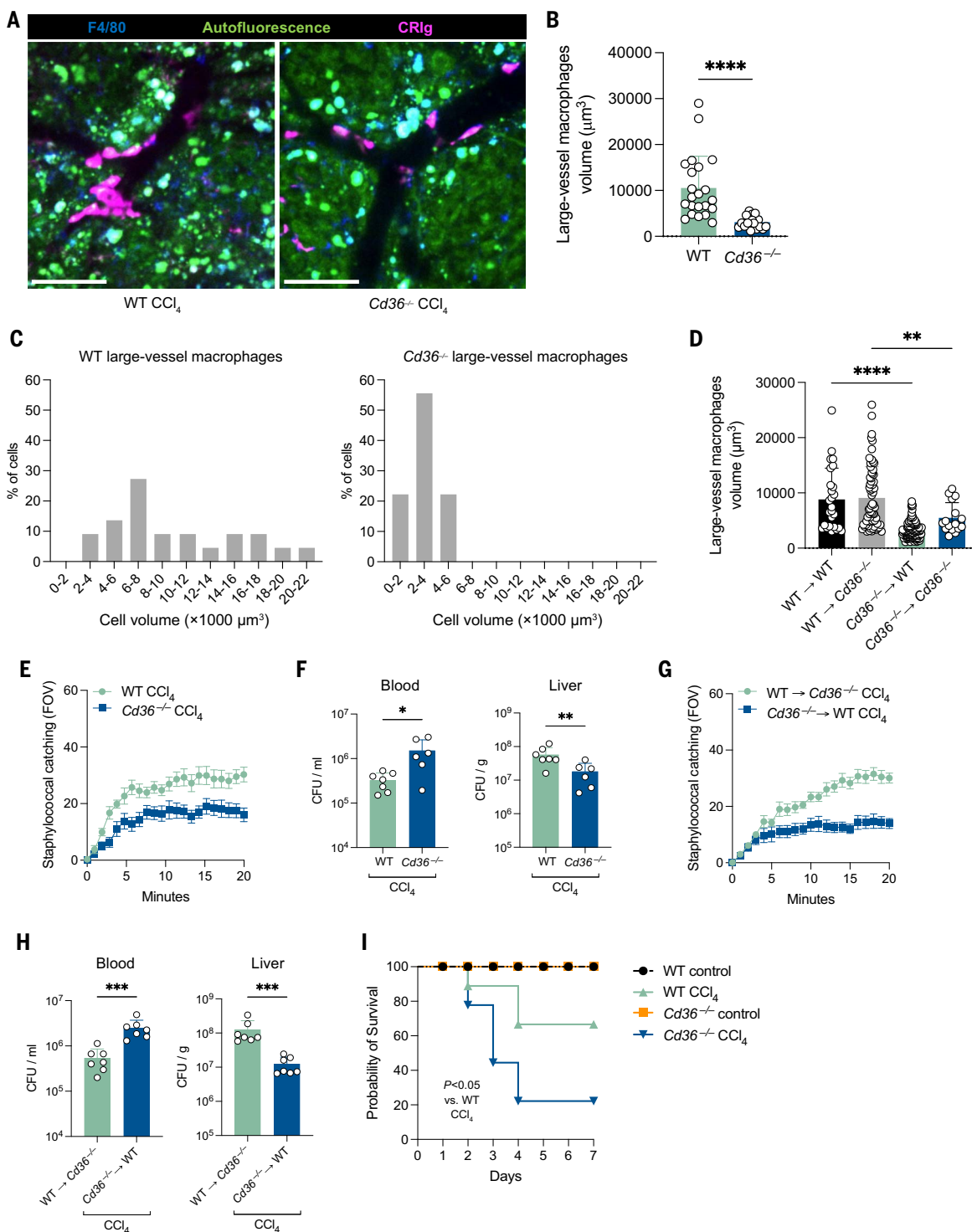


Fig. 7. Kupffer cell–like syncytia depend on the scavenger receptor CD36 for cell adhesion and fusion. (A) Representative IVM images of WT and Cd36^{-/-} mice treated with CCl₄ for 8 weeks. F4/80 (blue), CR Ig (magenta), hepatocytes (dull green), and tissue autofluorescence (bright green) are depicted. Scale bars: 75 μm. (B and C) Volumetric analysis of CR Ig-expressing macrophages in large vessels in WT and Cd36^{-/-} fibrotic mice ($n = 4$ per group, $N = 2$). (D) Volumetric analysis of CR Ig-expressing macrophages in large vessels in WT and Cd36^{-/-} bone marrow chimeric fibrotic mice ($n = 3$ to 5 per group, $N = 3$). (E) Enumeration of staphylococcal capture in WT and Cd36^{-/-} fibrotic mice infected with 5×10^7 CFU S. aureus MW2 ($n = 5$ per group, $N = 3$). (F) Bacterial

loads in WT and Cd36^{-/-} fibrotic mice infected with 5×10^7 CFU S. aureus MW2 ($n = 6$ or 7 per group, $N = 2$). (G) Quantification of staphylococcal capture in WT and Cd36^{-/-} bone marrow transplant experiments ($n = 3$ or 4 per group, $N = 2$). (H) Bacterial loads in WT and Cd36^{-/-} bone marrow transplant recipients ($n = 7$ per group, $N = 3$). (I) Survival analysis of WT and Cd36^{-/-} mice treated with CCl₄ for 8 weeks or controls and then infected with 5×10^7 CFU S. aureus MW2 ($n = 6$ to 8 per group, $N = 2$). Individual dots each represent one mouse in (F) and (H) and mean ± SEM in (E) and (G). Mann-Whitney test used for (B), (F), and (H). One-way ANOVA with Tukey post hoc test used in (D). Log-rank test used for survival study in (I). * $P < 0.05$, ** $P < 0.01$, *** $P < 0.001$, **** $P < 0.0001$.

presence of microbes or microbial products in the liver as well as high shear in these vessels cause monocytes to be recruited by CD44. They then fuse into syncytia mediated by CD36 and occupy a substantial part of the vessel lumen, a feature paramount for the capture of bacteria under flow conditions that have been altered by fibrosis. Moreover, a very profound relocation of stellate cells around the enlarged vessels perhaps helps impart KC characteristics to the KC-like syncytia, often capturing 10 times the number of bacteria that a single KC captures in its normal sinusoidal environment while maintaining tremendous microbial capacity.

Multinucleated giant cells were first described by Langerhans in tubercloid granulomas in 1868 (38) and have subsequently been identified in a number of pathologic settings, including foreign body responses, atherosclerosis, and autoimmunity (39). Giant cells in the bone form membrane fusions thought to increase their phagocytic capacity (32). In the liver, KCs have the critical task of capturing particulate matter under flow conditions, which notably precedes the process of phagocytosis. In larger vessels with much greater diameters, this task becomes insurmountable for a single macrophage, as was seen in *Cd36*^{-/-} mice. However, by increasing their size through bridging of multiple cells and filling a greater proportion of the lumen, these KC-like syncytia form a critical intravascular shield to help capture and eradicate bacteria in high-flow vessels. These cells presented as a continuum, ranging from clear clusters of abutting cells to true giant cells with a single membrane. Notably, KC-like syncytia did not block blood flow in a manner analogous to how KCs allow adequate flow in healthy sinusoids despite occupying a considerable proportion of the lumen.

Previous work on the KC niche determined that infiltrating monocytes have to contact LSECs, hepatocytes, and stellate cells, which then activate specific transcription factors to imprint KC identity (4, 24, 40). Within this framework, parenchymal cells provide instructive signals for KC development to fulfill their tissue-specific functions. We extend this work into disease states by showing that KCs in the context of fibrosis retract their many pseudopods and lose their instructive niche as sinusoids undergo fibrotic remodeling. These KCs downregulate important transcription factors including LXRx (Nr1h3) and downstream molecules such as CRIG and TIM-4. Previous single-cell RNA sequencing (RNA-seq) studies are consistent with these discoveries showing the increased heterogeneity of liver macrophages (12, 19).

Currently, 1.5 billion people worldwide live with chronic liver disease, and the burden is rising rapidly (41). Despite the importance of the liver as a microbial filter, most of these individuals do not suffer from bacteremia (42). Similarly, most fibrotic mice challenged with a

large intravenous bolus of pathogen survive infection, suggesting that a conserved presence of CRIG-expressing KC-like syncytia in fibrosis in both humans (43, 44) and rodents may be an adaptive mechanism to protect the host from infections. Although it is difficult to make the argument that alcoholic liver disease and nonalcoholic fatty liver disease have evolutionarily driven these adaptations for survival, liver trophic viruses that infect mammals may have spurred very similar evolutionary adaptations. Thus, the architectural reorganization of the liver disrupts the core constituents of the KC niche. This, in turn, drives an immune reorganization that may be a critical part of mammalian evolution by which the liver responds to severe chronic insults (viral, toxic, etc.) and prolongs organismal survival.

Materials and methods

Mice

All experiments were carried out using 8- to 12-week-old male and female mice. The experimental procedures were approved by the University of Calgary Animal Care Committee and were in accordance with Canadian Council for Animal Care Guidelines (Protocol No. AC-19-0138). All mice were cohoused and bred in a specific pathogen-free facility at the University of Calgary with a 12-hour light-dark cycle and access to food and water ad libitum. C56BL/6 mice (WT) were obtained from the Jackson Laboratory and subsequently bred in house. PepBoyJ (B6.SJL-Ptprc^aPepc^b/BoyJ, Jax: 002014), *Cx3cr1*^{CreER} [B6.129P2(Cg)-*Cx3cr1*^{tm2.1(cre)/ERT2}Litt/WganJ, Jax: 021160], Ai9 [B6.Cg-Gt(ROSA)26Sor^{tm1(CAG-tdTTomato)Hze}/J, Jax: 007909], *Cd44*^{-/-} [B6.129(Cg)-*Cd44*^{tm1Hbg}/J, Jax: 005085], *Cd36*^{-/-} [B6.129SI-*Cd36*^{tm1Mfe}/J, Jax: 019006], *Cx3cr1*^{gfp/+} [B6.129P2(Cg)-*Cx3cr1*^{tm1Litt}/J, Jax: 005582], Ai6 [B6.Cg-Gt(ROSA)26Sor^{tm6(CAG-ZsGreen)Hze}/J, Jax: 007906], *Rosa26*^{iDTR} [C57BL/6-Gt(ROSA)26Sor^{tm1(HBGF)Awai}/J, Jax: 007900], and *Myd88*^{-/-} [B6.129P2(SJL)-*Myd88*^{tm1.1Defr}/J, Jax: 009088] mice were purchased from the Jackson Laboratory and bred in house. *Clec4f*^{cre-nTdTTomato} mice (MGI Ref. ID: J:279524) were a kind gift from C. Glass (University of California, San Diego) and were crossed with Ai6 [B6.Cg-Gt(ROSA)26Sor^{tm6(CAG-ZsGreen)Hze}/J] mice to receive the dual reporter and with *Rosa26*^{iDTR} mice for specific ablation. *CRIG*^{-/-} mice (MGI Ref. ID: J:138691) were a kind gift from M. van Lookeren Campagne (Genentech). *Lrat*^{cre} mice (MGI Ref. ID: J:205330) were a kind gift from R. Schwabe (Columbia University, New York), and *Ms4a3*^{cre} mice (MGI Ref. ID: 284702) were provided by F.G. Both were crossed with Ai14 [B6.Cg-Gt(ROSA)26Sor^{tm14(CAG-tdTTomato)Hze}/J] mice.

Antibodies and reagents

All antibodies used in this study for IVM and flow cytometry are summarized in table S1.

Additional reagents used for IVM included labeling macrophages with the PKH26 Phagocytic Cell Labeling kit (Sigma-Aldrich) for long-term labeling of KCs, which was prepared according to the manufacturer's instructions. A dose of 100 μM was injected intravenously to label KCs. Tetramethyl rhodamine isothiocyanate (TRITC)-labeled Dextran (Invitrogen, Thermo Fisher Scientific) was used to visualize hepatic blood flow. Vybrant DiD Cell-Labeling Solution, pHrodo Red *Staphylococcus aureus* BioParticles, and Alexa Fluor 647 NHS Ester were obtained from Thermo Fisher Scientific. Tamoxifen and carbon tetrachloride were obtained from Sigma-Aldrich. Anti-CD9 antibody (clone ALB 6) was purchased from Santa Cruz Bioscience, isotype mouse IgG1 from BD Bioscience. Clodronate and phosphate-buffered saline (PBS) liposomes were obtained from <https://clodronateliposomes.com/>.

Bacterial strains and culture

S. aureus strain MW2 was obtained from the Network on Antimicrobial Resistance in *S. aureus* (NARSA) and transformed with pCM29 (45) to constitutively express green or yellow fluorescent protein (46). The MW2 strain was used for all experiments. Bacteria were cultured overnight in brain heart infusion medium (Difco) at 37°C on a shaker. Chloramphenicol (10 μg/ml) was added to the medium to maintain the plasmids. Bacteria were subcultured without antibiotics in brain heart infusion media until exponential phase growth was achieved (OD_{660nm} = 1.0), washed with saline, and resuspended in saline.

Mouse treatments

To induce liver fibrosis, mice were treated with 0.75 μl per gram of body weight of carbon tetrachloride (Sigma-Aldrich) dissolved in corn oil (Sigma-Aldrich) or corn oil alone by means of oral gavage three times a week for 8 weeks, unless otherwise specified. Mice were sacrificed 48 hours after the last dose. For infection experiments, mice were infected by tail vein injection of 5 × 10⁷ CFU *S. aureus* MW2 in 200 μl of saline. For survival studies, mice were infected with an intravenous injection of 5 × 10⁷ CFU *S. aureus* MW2 in 200 μl of saline. Infected mice were monitored closely, and their health status was assessed using an established scoring system (47). On the basis of this scoring system, mice were euthanized in cases where they reached their humane endpoint. KC depletion was performed as previously described (14). We injected 200 μl of clodronate liposomes (690 mM) via the tail vein 48 hours before the experiment or 200 μl of PBS liposomes for control groups. KCs in *Clec4f*^{cre-nTdTTomato} × *Rosa26*^{iDTR} mice were depleted by a single application of 10 ng per gram of body weight of diphtheria toxin (Sigma-Aldrich), as previously described (24). Anti-CD9 antibody (clone ALB 6) and IgG1

isotype were injected at a dose of 10 µg per mouse intraperitoneally three times per week for 8 weeks. Tamoxifen (Sigma-Aldrich) was dissolved in corn oil (Sigma-Aldrich) at 20 mg/ml and administered via intraperitoneal injection (100 µg per gram of body weight) for five consecutive days during indicated timepoints of CCl₄ administration.

Bacteriological analysis

Bacteriological analyses were performed after imaging experiments, 30 min after intravenous injection of bacteria, unless otherwise indicated. Anesthetized mice were washed and disinfected with 70% ethanol. Blood was collected by cardiac puncture into a heparinized syringe (100 U/ml). A liver lobe, spleen, lung lobe, and kidney were carefully removed, weighed, and homogenized using a tissue homogenizer. To assess colony-forming units, we serially diluted blood or tissue homogenate and then plated 30 µl onto brain heart infusion agar plates followed by incubation at 37°C. After 18 hours, bacterial colonies were counted.

Parabiosis

Parabiotic pairs were generated as previously described (48). Briefly, age-matched female mice were cohoused for 3 weeks before parabiosis surgery. For surgery, mice were anesthetized with an intraperitoneal injection of ketamine (200 µg per gram of body weight; Bayer Animal Health) and xylazine (10 µg per gram of body weight; Biomed-MTC) and placed under a sterile hood on a heating pad. A skin incision was made from shoulder levels to hips along lateral flanks on opposite sides. First, sutures were placed on shoulder and thigh skin and muscle layers and subsequently, sutures were completed along the incision of skin flaps using a stapler. Blood chimerism was assessed after 21 days of parabiosis by tail-vein cannulation and again after 8 weeks of CCl₄ treatment.

Depletion of commensal bacteria

Mouse intestinal commensal bacteria were depleted at birth with a cocktail of broad-spectrum antibiotics, as previously published (49). Mice were administered ampicillin (1 mg/ml), vancomycin (0.5 mg/ml), neomycin (1 mg/ml), metronidazole (1 mg/ml), and ciprofloxacin (0.2 mg/ml) via the drinking water. Antibiotics were purchased from Sigma-Aldrich.

Bone marrow transplantation

We performed two sets of experiments using bone marrow chimeras. In a first set of experiments, WT and Cd44^{-/-} mice were used, and in the second set, WT and Cd36^{-/-} mice were used. Each experiment included BM transfer controls (WT → WT, Cd44^{-/-} → Cd44^{-/-}, and Cd36^{-/-} → Cd36^{-/-}). Bone marrow was isolated from tibias and femurs of donor mice under sterile conditions. Recipient mice received

two doses of radiation of 5.25 grays (Gy) with a 3-hour interval between irradiations. Next, 8 × 10⁶ bone marrow cells were transferred via tail-vein injections. Mice were kept for 8 weeks to allow full bone marrow reconstitution.

Labeling of red blood cells

A donor mouse was sacrificed by cardiac puncture, and 500 µl of heparinized whole blood was obtained. Cells were then centrifuged at 400g for 10 min at room temperature, and plasma and leukocytes were discarded. RBCs were resuspended in 1 ml of RPMI medium (Thermo Fisher Scientific) supplemented with 2% fetal bovine serum. Cells were stained with 10 µl of DiD (Thermo Fisher Scientific) at room temperature for 10 min and then washed twice.

Mouse surgery for intravital microscopy of the liver

IVM was performed as previously published (50, 51). Mice were anesthetized using ketamine (200 µg per gram of body weight; Bayer Animal Health) and xylazine (10 µg per gram of body weight; Biomed-MTC) delivered by intraperitoneal injection. To gain intravenous access, a small catheter was inserted into the tail vein of mice. This allowed us to deliver fluorescently conjugated antibodies, bacteria for capture experiments, and additional anesthetics and fluids to maintain adequate hydration status of the mice. A surgical incision was made in the abdomen, and skin and abdominal muscle were partly removed. The liver was mobilized by cutting the attaching ligaments, while care was taken not to touch the liver to avoid tissue damage. Next, the mouse was placed in a lateral position on a heated microscopy stage with an inserted cover glass. The heated plate allowed us to maintain body temperature at 37°C. The liver was subsequently flipped onto the glass coverslip using a fine cotton tip to remove the intestines in a no-touch technique and then covered with wet laboratory tissues for stabilization. The mouse was wrapped in saline-soaked gauze and continuously hydrated by applying saline. During imaging, mice were regularly administered intravenous fluids and additional anesthetics.

Intravital microscopy of the liver

Images were acquired using an inverted spinning-disk confocal microscope (IX81; Olympus) that was equipped with a focus drive by Olympus and a motorized stage (Applied Scientific Instrumentation) to allow live movement in *x* and *y* axes. The microscope was stocked with a motorized objective turret fitted with 4X/0.16 UPLANSAPO, 10X/0.40 UPLANSAPO, and 20X/0.70 UPLANSAPO objective lenses. The microscope was placed onto an antivibration customized table (Newport, Irvine, CA). The spinning-disk confocal microscope was linked to a confocal light path (WaveFx; Quorum Tech-

nologies) that was based on a modified CSU-10 head (Yokogawa Electric Corporation). Laser excitation wavelengths were 491, 561, and 642 nm (Cobolt, Stockholm, Sweden), and a 512 pixel by 512 pixel back-thinned EMCCD camera (C9100-13, Hamamatsu, Bridgewater, NJ) was used for detection. Laser wavelengths were merged into an optic cable using an LMM5 laser merge module (Spectral Applied Research, Richmond Hill, Canada). Fluorescence visualization was through the bad-pass emission filters (Semrock, Rochester, NY) ET 525/50M, FF 593/40, and ET 700/75M and driven by a MAC 6000 Modular Automation Controller (Ludl Electronic Products, Hawthorne, NY). Volocity software (Quorum) was used to drive the confocal microscope and for acquisition and analysis of images. A combination of fluorescently conjugated antibodies, reporter mice, or fluorescent bacteria were used to visualize cells of interest and as functional readouts. For bacterial capture and imaging of particles, three to five fields of view (FOV) were randomly selected in the sinusoid area and three to five FOV in the venular region with the 10× objective and imaged for 20 min. For erythrocyte tracking, 1-min videos were obtained from a single point with low exposure time to allow for continuous imaging of flow. Collagen was imaged using a Leica SP8 DIVE inverted system with a multiphoton laser (52). An HC FLUOTAR L 25X/0.95 water immersion objective was used at 2× digital zoom. The microscope was equipped with a tunable InSight X3 ultrafast laser (Spectra-Physics), excited at 800 to 1000 nm and detected with external, extremely sensitive non-descanned hybrid detectors. Second-harmonic generation was imaged by tuning the detector to the excitation wavelength divided by two. LAS X software was used to drive the microscope.

Mechanical alteration of liver hemodynamics

To manipulate hepatic blood flow, we induced a mechanical stenosis of the portal vein. A small vascular clamp (Fine Surgical Tools, Vancouver, BC, Canada) was used, and a 4-0 Prolene suture (Ethicon) was tied around one end to prevent full occlusion. Mice were prepared for IVM as described. Before the liver was mounted onto the cover glass, the portal vein was identified, and the clamp was carefully applied. In some experiments, as indicated, the clamp was removed during live imaging to restore blood flow.

Intravital microscopy of the lung

Lung IVM was performed as described previously (30). Briefly, anesthetized mice were placed on a heating pad. A tracheotomy was performed, and mice were ventilated using a small rodent ventilator (Harvard Apparatus). After the mouse was placed in a lateral position, a small intercostal incision was applied, and a custom-made intercostal lung window was inserted. Lung tissue was stabilized using suction of 20 mmHg.

Images were acquired using an upright microscope (BX51, Olympus) equipped with a confocal light path (WaveFx, Quorum, ON, Canada) and a back-thinned electron multiplying charge-coupled device camera (Hamamatsu Photonics) for fluorescence detection. Lung macrophages were visualized by intratracheal injection of 0.5 μ M PKH26 (Sigma Aldrich, Darmstadt, Germany) and intravenous injection of fluorescently labeled anti-CX3CR1 monoclonal antibody (1 μ g per mouse; clone SA011F11; Biolegend).

Intravital microscopy of the spleen

Spleen IVM was performed as previously described (48). In brief, a skin incision was made, the mouse was placed in a left lateral position, and the spleen was exteriorized onto a cover glass and fixed with wet laboratory tissue paper. A suture was placed in the attached fat tissue to stabilize the spleen on the cover glass. Red-pulp macrophages and vasculature were visualized using fluorescently labeled antibodies against CD31 and F4/80 (table S1). Images were acquired using an inverted spinning disk confocal microscope (IX81; Olympus), which was coupled with a confocal light path (WaveFx, Quorum, ON, Canada), a focus drive, and a motorized stage (Applied Scientific Instrumentation). A back-thinned electron multiplying charge-coupled device camera (Hamamatsu Photonics) was used for fluorescence detection, and Volocity Software (Quorum, ON, Canada) was used to drive the microscope.

In vivo phagocytosis assay

Phagocytosis and lysosome acidification of liver macrophages were assessed as previously described (15). Following the manufacturer's instructions, pHrodo Red S. aureus BioParticles (2 mg/ml) were stained with 50 μ g/ml of Alexa Fluor 647 NHS ester in 100 mM bicarbonate-buffered saline (pH 8.3) for 30 min at room temperature. For IVM, fields of view were chosen, and a baseline was recorded for 1 min before injection of bioparticles (40 μ g per mouse). The pHrodo and AF647 signals were visualized for 60 min. Volocity software was used to quantify uptake and percentage of acidified particles. The bioparticles were labeled with AF647 as a reference color, and acidification of the bioparticles in low pH environment in phagolysosomes was indicated by an increase in pHrodo in the caught and internalized bioparticles.

Isolation of hepatic leukocytes

Liver leukocytes were isolated as previously described (50). In brief, the inferior vena cava was cannulated, and the liver was perfused *in situ*, first with Ca^{2+} -, Mg^{2+} -free Hank's Balanced Salt Solution (HBSS, Thermo Fisher Scientific) and then with HBSS containing 0.05% collagenase type IV (Worthington Biomedical, Lakewood, NJ) and 0.02% DNase I

(Roche) at a flow rate of 4 ml/min using a peristaltic pump. The liver was subsequently removed and digested in HBSS containing 0.009% collagenase type IV and 0.02% DNase I at 37°C for 30 min on a shaker. The suspension was then passed through a 100- μ m cell strainer (BD Bioscience) and centrifuged at 25g for 5 min at room temperature to remove debris and hepatocytes. The supernatant was collected and centrifuged at 400g for 10 min at 4°C. The cells were then resuspended in 15% iodixanol solution (Sigma-Aldrich) and centrifuged at 400g for 15 min at room temperature without a break. The band of non-parenchymal cell fraction was aspirated using a transfer pipet and washed twice with HBSS. After a step of red blood cell lysis using ACK (ammonium-chloride-potassium) lysis buffer (Thermo Fisher Scientific), the cells of interest were resuspended in 100 μ l of flow buffer [PBS with 0.5% bovine serum albumin (BSA) and 2 mM EDTA].

Flow cytometry

Resuspended cells were first blocked using anti-mouse CD16/32 antibody (2.4G2, BioXcell) for 10 min. Cells were then stained with specific markers for 30 min at 4°C, and appropriate isotype antibodies and FMO controls were used. Nonviable cells were labeled using viability dye Ghost Dye red 710 (TONBO Bioscience). After staining, cells were washed and fixed in 1% paraformaldehyde (PFA). Spectral multicolor flow cytometry was performed immediately after staining without fixing cells. The samples were acquired using a BD FACS Canto II flow cytometer or a spectral flow cytometer (Aurora, Cytek) and analyzed using FlowJo software (Tree Star). Cells were gated on forward scatter/side scatter, singlets, live, and CD45^+ to identify leukocytes. Subsequently, neutrophils were identified as CD45^+ Ly6G^+ cells and non-granulocytes were analyzed further after exclusion of SiglecF $^+$ cells and CD19^+ cells. Cell populations from multiple mice per group (control and CCl₄) were concatenated, and simultaneous tSNE analyses were performed.

Isolation and ex vivo imaging of liver macrophages

Single-cell liver suspensions were generated as described above, except cells were not passed through a filter. Instead, single-cell suspensions were placed in a 15-ml canonical tube and allowed to rest for 5 min at room temperature to sediment debris and hepatocytes. Supernatant was aspirated, and debris and hepatocytes discarded. The supernatant was centrifuged for 10 min at 400g. Cells were then resuspended in 15% iodixanol solution and centrifuged at 400g for 15 min at room temperature without a break. Cells were resuspended in Ca^{2+} -, Mg^{2+} -free Hank's balanced salt solution (HBSS, Thermo Fisher Scientific). Nonparenchymal liver cells were collected and stained with F4/80 anti-

bodies and Hoechst nuclear dye (Invitrogen, Thermo Fisher Scientific) in a buffer containing 0.5% BSA and 2 mM EDTA. Cells were fixed for 10 min in 4% paraformaldehyde. Single-cell suspensions were mounted on a coverslip and imaged immediately on a Leica SP8 DIVE inverted system using the 65 \times water immersion objective in high magnification.

Transmission electron microscopy

Mice were sacrificed and the liver was excised. Punch biopsies were obtained (1 mm by 3 mm) and fixed in a solution of 1.6% paraformaldehyde and 2.5% glutaraldehyde in 0.1 M cacodylate buffer. Sections were dehydrated through an ethanol series and embedded in epon mixture. The epon layer with tissue was removed after polymerizing. A representative area was identified using a light microscope and glued to resin stub for sectioning. Fine sections were cut using an ultramicrotome with a diamond knife and collected on single-hole grids with Formvar support. Sections were subsequently stained with aqueous uranyl acetate and Reynold's lead citrate. Images were acquired with a Hitachi H7650 TEM at 80 kV equipped with a AMT16000 digital camera.

Human samples

Human liver tissue was obtained from three major transplant hepatology centers: the Department of Hepatobiliary and Transplant Surgery, University Medical Center Hamburg-Eppendorf, Hamburg, Germany; Charité University Medicine, Berlin, Germany; and the Multi-Organ Transplant Program, Toronto General Hospital Research Institute, University of Toronto, Toronto, Canada. Healthy tissue was obtained from neurologically deceased donors whose livers were determined to be acceptable for transplantation. Cirrhotic tissue was obtained from explant livers or patients undergoing liver biopsy. The etiology of cirrhosis of the patients included was alcoholic liver disease ($n = 4$), nonalcoholic fatty liver disease ($n = 5$), hepatitis B virus infection ($n = 1$), primary sclerosing cholangitis ($n = 5$), and primary biliary cholangitis ($n = 1$). All patients provided written informed consent. Study was approved by the Institutional Review Board of the medical faculty at the University of Hamburg (PV4898), the Ethics Committee at Charité University Medicine Berlin (Project EA2/091/19), and the institutional Research Ethics Board in Toronto (REB #14-7425 and REB # 20-5142) and conducted according to the ethical principles of the Declaration of Helsinki and its revised versions.

Immunohistochemistry of human liver tissue

Formalin-fixed paraffin-embedded (FFPE) liver tissues were sectioned (4- μ m sections) and then stained with hematoxylin and eosin (H&E), trichrome, or anti-human CD68 according to

the standard histological procedures. Additional antibodies used for immunohistochemistry were anti-IBA1 (clone 20A12.1, Merck, Germany), anti-sodium potassium adenosine triphosphatase (ATPase) antibody (clone 464.6, Abcam, USA), anti-Heppar1 (clone OCHIE5, Dako, Denmark), and anti-VSIG4 (clone EPR22576-125, Abcam, USA).

Immunofluorescence staining of liver cryosections

Liver tissues were embedded in cryo molds using Shandon Cryochrome (ThermoFisher Scientific), and 5- μ m tissue sections were prepared. Tissue slides were fixed and permeabilized in acetone for 10 min at room temperature. Tissue sections were washed three times with PBS and blocked by incubating with 10% BSA/PBS for 30 min at RT. Subsequently, tissue sections were incubated with the primary antibodies CD68-PE (clone: JO127; Santa Cruz; dilution: 1:100) and VSIG4-APC (CRIg) (clone: JAV4, eBioscience; dilution: 1:100) overnight at 4°C. Tissue sections were washed three times with 0.1% BSA/PBS and stained with Hoechst 34580 (Sigma-Aldrich; dilution: 1:2000) for 15 min at RT. Tissue sections were mounted using fluorescein mounting media (Dako, Glostrup, Denmark) and imaged using an Nikon A1 confocal microscope equipped with a 40 \times NA 1.15 water immersion long-working-distance objective.

Fibrosis assessment

Livers were fixed in 10% formalin and sent to Calgary Laboratory Services for paraffin embedding, sectioning, and staining of Sirius Red. Slides were imaged using a Thorlabs Whole-Slide-Scanning microscope. Sirius Red staining was quantified using ImageJ (53).

Image analysis and processing

Image analysis was done using Volocity Software (Quorum), ImageJ (NIH), or Imaris Software (Bitplane). Immunofluorescence data was analyzed using ImageJ, images were exported as .tif and further analyzed using ImageJ (NIH). Bacterial capture experiments were assessed using Volocity software as previously described (15) in automated fashion using the “find objects” function with the same threshold settings throughout. Background autofluorescence was assessed before injection of bacteria and subtracted from the results. Percentage of acidified particles was calculated from the total number of captured bioparticles with the reference color and the particles that over time turned red. For the measurement of sinusoid and venule diameters, images were exported from Volocity software as .tif files. ImageJ software (NIH) was used to measure diameters. We measured 10 randomly selected sinusoids and venules in five fields of view (FOV) per mouse. Syncytia quantity was performed using computer-generated stitch images exported from Volocity. Liver surface area was determined,

and syncytia were counted manually on the basis of intravascular location and CRIg and F4/80 coexpression. Blood velocity was quantified using the automated tracking function in Volocity. A protocol was generated using the “find objects” and “track” tasks from the measurement modality, and labeled RBCs were tracked over a 1-min video. RBCs were assigned to their respective locations in sinusoids or venules and static events were excluded. Only RBCs that were trackable over 100 timepoints were included at an imaging speed of 10 frames per second. Three-dimensional (3D) reconstructions were generated using the “3D opacity” function in Volocity. Quantification of intravascular macrophages was performed in ImageJ using the image calculator function to count cells coexpressing F4/80 and CX3CR1 in the selected region of interest (ROI; venule) and expressed as percentage of surface area covered. Analysis of KC morphology, expression of KC markers, distribution of *S. aureus*, frequency of Ms4a3-labeling, frequency of CLEC4F nuclear signal and cytosolic signal, and frequency of PKH labeling and KC chimerism in parabiosis experiments was performed in Volocity software using the object counting tool. Three to five randomly selected FOV were assessed, the total number of KCs, and number of KCs expressing respective markers were quantified and expressed as percentage of total per FOV. The analysis was restricted to KC located in liver sinusoids. Volumetric analysis was done using Volocity software. Liver macrophage volume was assessed using computer-generated 3D renderings of 1- μ m z-stack images. KC-like syncytia were identified on the basis of intravascular location in large vessels and coexpression of F4/80 and CRIg. Sinusoidal macrophage subsets were identified on the basis of their intravascular location in sinusoids and their respective expression of F4/80, CRIg, and TIM-4. We assessed five FOVs per mouse for KC-like syncytia and five randomly selected FOVs per mouse for macrophage subtypes in sinusoids. HSC and sinusoidal macrophage interaction was quantified using the “extended focus” function with z-stack images in Volocity software. A protocol was generated, using the “find objects” task from the measurement modality to identify all HSCs in the FOV. Second, an ROI was manually generated for each macrophage. Third, using the “intersect” task, objects and ROIs were combined to assess the surface area of individual macrophages covered by HSCs. The surface area of macrophages interacting with HSCs were then normalized to percentage of cell surface in contact with HSCs. Three to five FOVs were assessed per mouse. For all imaging quantifications, multiple FOV were assessed and averaged to count each mouse as $n = 1$. CRIg expression in human cirrhosis was quantified using ImageJ in automated fashion using the “analyze particles” task. Three to five

randomly selected FOV were chosen, and coexpression of CRIg and IBA1 was then enumerated. Cell size in human liver tissues was analyzed as previously described (54). In brief, single-field images were acquired using a Zeiss Axio Observer 7. Large-field scanned images were stitched and further processed in ImageJ. Hyperstacks were concatenated and aligned. Cell identification, counting, distribution, and size measurement were performed using CellProfiler.

RNA sequencing

Eight samples in total (five controls and three CCl₄-treated) were analyzed for bulk RNA-seq. After isolation of hepatic leukocytes, 2×10^5 of embryonic KCs (F4/80^{hi}CD11b^{lo}Ms4a3⁻) were purified by fluorescence-activated cell sorting and placed into 500 μ l of QIAzol lysis buffer (QIAGEN, Venlo, Netherlands). Total RNA was isolated using a RNeasy Plus micro kit (QIAGEN, Venlo, Netherlands) and sent to the Centre for Health Genomics facility at the University of Calgary, where the RNA-seq was performed using a NextSeq sequencer (Illumina, San Diego, CA, USA). Total RNA was preprocessed to remove ribosomal RNA using NEBNext Ultra II Directional RNA Library Prep Kit for Illumina with rRNA depletion (New England Biolabs, Ipswich, MA, USA). The libraries were quantified by quantitative polymerase chain reaction using the KAPA Library Quantification Kit for Illumina with equimolar pooling and sequenced on a NextSeq 500 High output 75-cycle run. All samples passed the quality control for the library prep and sequence run metrics.

Analysis of RNA-seq data

Five control samples and three CCl₄-treated samples (including one pool of two unique treated samples owing to minimum sequencing library input requirements) were quantified using Kallisto v0.42.4 (55) against the NCBI RefSeq murine transcriptome (GRCm38). A linear regression model was used to determine differentially expressed transcripts using treatment (0 or 1) as the experimental variable. Differentially expressed genes were considered those with a false discovery rate (Benjamini-Hochberg-corrected $P < 0.05$) under the Wald test in Sleuth v0.30.0 (56) and a minimum of 40 raw reads mapped. Differentially expressed transcripts were subsequently annotated and analyzed using Ingenuity Pathway Analysis (Qiagen, Redwood City, CA) Core Analysis. DESeq2 was used to apply a negative binomial generalized linear model to determine differentially expressed genes between control and treatment groups (57). DESeq2 was used to generate PCA plots, and heatmaps were generated using the ComplexHeatmap package (58).

Analysis of single-cell RNA-seq data

The dataset used to interrogate gene expression of macrophages and monocytes in the CCl₄ model

was previously published (12) and is accessible in the GEO database (GSE136103). In this study, mice were first treated with CCl₄. Liver leukocytes were sorted and then processed for droplet-based single-cell RNA-seq. Mononuclear phagocytes were clustered according to the initial study in five clusters. Genes of interest were analyzed and displayed.

Statistical analysis

The sample size was predetermined before investigation on the basis of experience with similar hypothesis testing experiments. All data are represented as individual values with mean ± SD unless otherwise indicated in the figure legend. Generally, each data point is one biological replicate (*n*). The number of times an experiment was independently repeated (*N*) and the number of biological replicates (*n*) is stated in the figure legends. Statistical analyses were performed using GraphPad Prism (Version 8.0). Normality distribution was assessed and comparison of two groups was done either with unpaired Student's *t* test (two-tailed) or Mann-Whitney test, as appropriate. When assessing three or more groups, one-way analysis of variance (ANOVA) with Tukey's post hoc test was performed. Statistical significance was set at *P* < 0.05.

REFERENCES AND NOTES

- C. N. Jenne, P. Kubes, Immune surveillance by the liver. *Nat. Immunol.* **14**, 996–1006 (2013). doi: 10.1038/ni.2691; pmid: 24048121
- T. Huby, E. L. Gautier, Immune cell-mediated features of non-alcoholic steatohepatitis. *Nat. Rev. Immunol.* **22**, 429–443 (2022). doi: 10.1038/s41577-021-00639-3; pmid: 34741169
- F. Heymann, F. Tacke, Immunology in the liver—From homeostasis to disease. *Nat. Rev. Gastroenterol. Hepatol.* **13**, 88–110 (2016). doi: 10.1038/nrgastro.2015.200; pmid: 26758786
- J. Bonnardel et al., Stellate cells, hepatocytes, and endothelial cells imprint the Kupffer cell identity on monocytes colonizing the liver macrophage niche. *Immunity* **51**, 638–654.e9 (2019). doi: 10.1016/j.jimmuni.2019.08.017; pmid: 31561945
- Y. Iwakiri, V. Shah, D. C. Rockey, Vascular pathobiology in chronic liver disease and cirrhosis – current status and future directions. *J. Hepatol.* **61**, 912–924 (2014). doi: 10.1016/j.jhep.2014.05.047; pmid: 24911462
- J. Gracia-Sancho, G. Marrone, A. Fernández-Iglesias, Hepatic microcirculation and mechanisms of portal hypertension. *Nat. Rev. Gastroenterol. Hepatol.* **16**, 221–234 (2019). doi: 10.1038/s41575-018-0097-3; pmid: 30568278
- D. Schuppan, N. H. Afshar, Liver cirrhosis. *Lancet* **371**, 838–851 (2008). doi: 10.1016/S0140-6736(08)60383-9; pmid: 18328931
- M. J. Lane, R. B. Jeffrey Jr., D. S. Katz, Spontaneous intrahepatic vascular shunts. *AJR Am. J. Roentgenol.* **174**, 125–131 (2000). doi: 10.2214/ajr.174.1.1740125; pmid: 10628467
- E. M. Remer, G. A. Motta-Ramirez, J. M. Henderson, Imaging findings in incidental intrahepatic portal venous shunts. *AJR Am. J. Roentgenol.* **188**, W162–W167 (2007). doi: 10.2214/AJR.05.1115; pmid: 17242223
- M. Praktikno et al., Total area of spontaneous portosystemic shunts independently predicts hepatic encephalopathy and mortality in liver cirrhosis. *J. Hepatol.* **72**, 1140–1150 (2020). doi: 10.1016/j.jhep.2019.12.021; pmid: 31954206
- T. Su et al., Single-cell transcriptomics reveals zone-specific alterations of liver sinusoidal endothelial cells in cirrhosis. *Cell. Mol. Gastroenterol. Hepatol.* **11**, 1139–1161 (2021). doi: 10.1016/j.cmgch.2020.12.007; pmid: 33340713
- P. Ramachandran et al., Resolving the fibrotic niche of human liver cirrhosis at single-cell level. *Nature* **575**, 512–518 (2019). doi: 10.1038/s41586-019-1631-3; pmid: 31597160
- I. Mederacke et al., Fate tracing reveals hepatic stellate cells as dominant contributors to liver fibrosis independent of its aetiology. *Nat. Commun.* **4**, 2823 (2013). doi: 10.1038/ncomms3823; pmid: 24264436
- B. G. Surewaerd et al., Identification and treatment of the *Staphylococcus aureus* reservoir in vivo. *J. Exp. Med.* **213**, 1141–1151 (2016). doi: 10.1084/jem.20160334; pmid: 27325887
- B. G. J. Surewaerd, P. Kubes, Measurement of bacterial capture and phagosome maturation of Kupffer cells by intravital microscopy. *Methods* **128**, 12–19 (2017). doi: 10.1016/j.jymeth.2017.05.004; pmid: 28522327
- M. Guilliams, C. L. Scott, Liver macrophages in health and disease. *Immunity* **55**, 1515–1529 (2022). doi: 10.1016/j.jimmuni.2022.08.002; pmid: 36103850
- K. Y. Helmy et al., CRIG: A macrophage complement receptor required for phagocytosis of circulating pathogens. *Cell* **124**, 915–927 (2006). doi: 10.1016/j.cell.2005.12.039; pmid: 16530040
- Z. Zeng et al., CRIG functions as a macrophage pattern recognition receptor to directly bind and capture blood-borne Gram-positive bacteria. *Cell Host Microbe* **20**, 99–106 (2016). doi: 10.1016/j.chom.2016.06.002; pmid: 27345697
- A. Remmerie et al., Osteopontin expression identifies a subset of recruited macrophages distinct from Kupffer cells in the fatty liver. *Immunity* **53**, 641–657.e14 (2020). doi: 10.1016/j.jimmuni.2020.08.004; pmid: 32888418
- J. S. Seidman et al., Niche-specific reprogramming of epigenetic landscapes drives myeloid cell diversity in nonalcoholic steatohepatitis. *Immunity* **52**, 1057–1074.e7 (2020). doi: 10.1016/j.jimmuni.2020.04.001; pmid: 32362324
- S. Tran et al., Impaired Kupffer cell self-renewal alters the liver response to lipid overload during non-alcoholic steatohepatitis. *Immunity* **53**, 627–640.e5 (2020). doi: 10.1016/j.jimmuni.2020.06.003; pmid: 32562600
- Z. Liu et al., Fate mapping via Ms4a3-expression history traces monocyte-derived cells. *Cell* **178**, 1509–1525.e19 (2019). doi: 10.1016/j.cell.2019.08.009; pmid: 31491389
- E. Mass et al., Specification of tissue-resident macrophages during organogenesis. *Science* **353**, aaf4238 (2016). doi: 10.1126/science.aaf4238; pmid: 27492475
- M. Sakai et al., Liver-derived signals sequentially reprogram myeloid enhancers to initiate and maintain Kupffer cell identity. *Immunity* **51**, 655–670.e8 (2019). doi: 10.1016/j.jimmuni.2019.09.002; pmid: 31587991
- C. L. Scott et al., The transcription factor ZEB2 is required to maintain the tissue-specific identities of macrophages. *Immunity* **49**, 312–325.e5 (2018). doi: 10.1016/j.jimmuni.2018.07.004; pmid: 30076102
- A. Guillot et al., Bile acid-activated macrophages promote biliary epithelial cell proliferation through integrin αvβ6 upregulation following liver injury. *J. Clin. Invest.* **131**, e132305 (2021). doi: 10.1172/JCI132305; pmid: 33724957
- K. R. Karlmark et al., Hepatic recruitment of the inflammatory Gr1⁺ monocyte subset upon liver injury promotes hepatic fibrosis. *Hepatology* **50**, 261–274 (2009). doi: 10.1002/hep.22950; pmid: 19554540
- S. Yona et al., Fate mapping reveals origins and dynamics of monocytes and tissue macrophages under homeostasis. *Immunity* **38**, 79–91 (2013). doi: 10.1016/j.jimmuni.2012.12.001; pmid: 23273845
- F. F. Hoyer et al., Tissue-specific macrophage responses to remote injury impact the outcome of subsequent local immune challenge. *Immunity* **51**, 899–914.e7 (2019). doi: 10.1016/j.jimmuni.2019.10.010; pmid: 31732166
- A. S. Neupane et al., Patrolling alveolar macrophages conceal bacteria from the immune system to maintain homeostasis. *Cell* **183**, 110–125.e11 (2020). doi: 10.1016/j.cell.2020.08.020; pmid: 3288431
- R. Wiest, M. Lawson, M. Geuking, Pathological bacterial translocation in liver cirrhosis. *J. Hepatol.* **60**, 197–209 (2014). doi: 10.1016/j.jhep.2013.07.044; pmid: 23993913
- L. Helmung, S. Gordon, Molecular mediators of macrophage fusion. *Trends Cell Biol.* **19**, 514–522 (2009). doi: 10.1016/j.tcb.2009.07.005; pmid: 19733078
- H. A. Crosby, P. F. Lalor, E. Ross, P. N. Newsome, D. H. Adams, Adhesion of human haematopoietic (CD34⁺) stem cells to human liver compartments is integrin and CD44 dependent and modulated by CXCR3 and CXCR4. *J. Hepatol.* **51**, 734–749 (2009). doi: 10.1016/j.jhep.2009.06.021; pmid: 19703720
- Y. Hou, Q. Zou, R. Ge, F. Shen, Y. Wang, The critical role of CD133⁺CD44^{+high} tumor cells in hematogenous metastasis of liver cancers. *Cell Res.* **22**, 259–272 (2012). doi: 10.1038/cr.2011.139; pmid: 21862973
- B. McDonald et al., Interaction of CD44 and hyaluronan is the dominant mechanism for neutrophil sequestration in inflamed liver sinusoids. *J. Exp. Med.* **205**, 915–927 (2008). doi: 10.1084/jem.20071765; pmid: 18362172
- C. Shi et al., Monocyte trafficking to hepatic sites of bacterial infection is chemokine independent and directed by focal intercellular adhesion molecule-1 expression. *J. Immunol.* **184**, 6266–6274 (2010). doi: 10.4049/jimmunol.0904160; pmid: 20435926
- O. Krenkel, F. Tacke, Liver macrophages in tissue homeostasis and disease. *Nat. Rev. Immunol.* **17**, 306–321 (2017). doi: 10.1038/nri.2017.11; pmid: 28317925
- T. Langhans, Ueber Riesenzenellen mit wandständigen Kernen in Tuberkeln und die fibröse Form des Tuberkels. *Virchows Arch.* **42**, 382–404 (1868). doi: 10.1007/BF02006420
- M. T. Quinn, I. A. Schepetkin, Role of NADPH oxidase in formation and function of multinucleated giant cells. *J. Innate Immun.* **1**, 509–526 (2009). doi: 10.1159/000228158; pmid: 20375608
- M. Guilliams, C. L. Scott, Does niche competition determine the origin of tissue-resident macrophages? *Nat. Rev. Immunol.* **17**, 451–460 (2017). doi: 10.1038/nri.2017.42; pmid: 28461703
- A. M. Moon, A. G. Singal, E. B. Tapper, Contemporary epidemiology of chronic liver disease and cirrhosis. *Clin. Gastroenterol. Hepatol.* **18**, 2650–2666 (2020). doi: 10.1016/j.cgh.2019.07.060; pmid: 31401364
- A. Martini, E. Ceranto, A. Gatta, P. Angelis, P. Pontisso, Occult liver disease burden: Analysis from a large general practitioners' database. *United European Gastroenterol. J.* **5**, 982–986 (2017). doi: 10.1177/2050640617696402; pmid: 29163964
- J. Lewis, Histopathology of granulomatous liver disease. *Clin. Liver Dis. (Hoboken)* **11**, 77–80 (2018). doi: 10.1002/cld.695; pmid: 30992794
- H. Zhu, H. C. Bodenheimer Jr., D. J. Clain, A. D. Min, N. D. Theise, Hepatic lipogranulomas in patients with chronic liver disease: Association with hepatitis C and fatty liver disease. *World J. Gastroenterol.* **16**, 5065–5069 (2010). doi: 10.3748/wjg.v16.i40.5065; pmid: 20976843
- Y. Y. Pang et al., agr-Dependent interactions of *Staphylococcus aureus* USA300 with human polymorphonuclear neutrophils. *J. Innate Immun.* **2**, 546–559 (2010). doi: 10.1159/000319855; pmid: 20829608
- B. G. Surewaerd et al., Inactivation of staphylococcal phenol soluble modulins by serum lipoprotein particles. *PLOS Pathog.* **8**, e1002606 (2012). doi: 10.1371/journal.ppat.1002606; pmid: 22457627
- B. Shurin et al., A robust scoring system to evaluate sepsis severity in an animal model. *BMC Res. Notes* **7**, 233 (2014). doi: 10.1186/1756-0500-7-233; pmid: 24275742
- J. F. Deniset, B. G. Surewaerd, W. Y. Lee, P. Kubes, Splenic Ly6G^{high} mature and Ly6G^{int} immature neutrophils contribute to eradication of *S. pneumoniae*. *J. Exp. Med.* **214**, 1333–1350 (2017). doi: 10.1084/jem.20161621; pmid: 28424248
- M. Honda et al., Perivascular localization of macrophages in the intestinal mucosa is regulated by Nr4a1 and the microbiome. *Nat. Commun.* **11**, 1329 (2020). doi: 10.1038/s41467-020-15068-4; pmid: 32165624
- C. Deppermann et al., Tacrolimus impairs Kupffer cell capacity to control bacteremia: Why transplant recipients are susceptible to infection. *Hepatology* **73**, 1967–1984 (2021). doi: 10.1002/hep.31499; pmid: 32761929
- W. Y. Lee et al., An intravascular immune response to *Borrelia burgdorferi* involves Kupffer cells and iNKT cells. *Nat. Immunol.* **11**, 295–302 (2010). doi: 10.1038/ni.1855; pmid: 20228796
- J. Zindel et al., Primordial GATA6 macrophages function as extravascular platelets in sterile injury. *Science* **371**, eabe0595 (2021). doi: 10.1126/science.abe0595; pmid: 33674464
- J. Schindelin et al., Fiji: An open-source platform for biological-image analysis. *Nat. Methods* **9**, 676–682 (2012). doi: 10.1038/nmeth.2019; pmid: 22743772
- A. Guillot et al., Mapping the hepatic immune landscape identifies monocytic macrophages as key drivers of steatohepatitis and cholangiopathy progression. *Hepatology* **78**, 150–166 (2023). doi: 10.1097/HEP.0000000000000270; pmid: 36630995
- N. L. Bray, H. Pimentel, P. Melsted, L. Pachter, Near-optimal probabilistic RNA-seq quantification. *Nat. Biotechnol.* **34**, 525–527 (2016). doi: 10.1038/nbt.3519; pmid: 27043002
- H. Pimentel, N. L. Bray, S. Puente, P. Melsted, L. Pachter, Differential analysis of RNA-seq incorporating quantification uncertainty. *Nat. Methods* **14**, 687–690 (2017). doi: 10.1038/nmeth.4324; pmid: 28581496

57. M. I. Love, W. Huber, S. Anders, Moderated estimation of fold change and dispersion for RNA-seq data with DESeq2. *Genome Biol.* **15**, 550 (2014). doi: [10.1186/s13059-014-0550-8](https://doi.org/10.1186/s13059-014-0550-8); pmid: [25516281](#)
58. Z. Gu, R. Els, M. Schlesner, Complex heatmaps reveal patterns and correlations in multidimensional genomic data. *Bioinformatics* **32**, 2847–2849 (2016). doi: [10.1093/bioinformatics/btw313](https://doi.org/10.1093/bioinformatics/btw313); pmid: [27207943](#)
59. M. Peiseler *et al.*, Kupffer cell-like syncytia replenish resident macrophage function in fibrotic liver, Dryad (2023); <https://doi.org/10.5061/dryad.3ffbg79pp>.

ACKNOWLEDGMENTS

We thank L. Zbytniuk, M. Newton, and T. Nussbaumer for excellent technical support. We thank K. Poon for assistance with flow cytometry. We thank all current and past Kubes lab members for constant support and feedback. The authors thank L. Babes for help with IVM. We thank the Centre for Health Genomics and Informatics for help with RNA-seq. **Funding:** M.P. is supported by the German Research Foundation (DFG, PE2737/1-1) and is a member of the Berlin Institute of Health (BIH) Clinician Scientist Program; B.A.D. is supported by the Beverly Phillip's fellowship; J.Z. is supported by the Swiss National Science Foundation (SNSF P1BEP3_181164); J.D. and B.G.J.S. are supported by fellowships from the Canadian Institute of Health Research (CIHR); F.V.S.C. is supported by a fellowship from Canadian Institute of Health Research (MFE-176551); R.S. is a

Cancer Research Institute Irvington Fellow supported by the Cancer Research Institute (CRI4653); Y.N. is a Robert Black Fellow of the Damon Runyon Cancer Research Foundation, DRG-2401-20; K.M. is funded by the Canadian Institute of Health Research (CIHR); and P.K. is supported by the NSERC Discovery grant (RGPIN/07191-2019), the Heart and Stroke Foundation of Canada, CIHR, and Canada Research Chairs Program. **Author contributions:** M.P. designed and performed the experiments, analyzed data, wrote the manuscript, and designed figures. B.A.D. performed flow cytometry and imaging experiments, analyzed data, and designed figures. P.K. supervised the study, designed experiments, obtained funding, and wrote the manuscript. J.Z. analyzed RNA-seq data and helped with image data analysis. B.G.J.S. performed imaging experiments and helped design experiments. W.-Y.L. performed imaging experiments. Y.N. conducted flow cytometry experiments. F.V.S.C. performed lung imaging. R.S. performed imaging experiments. J.D. helped design experiments. C.O. and K.M. provided GF mice and assisted with experiments. P.G.M. performed electron microscopy experiments, and P.G.M. and M.Am. helped analyze electron microscopy data. F.H. analyzed flow experiments and acquired human images and helped with image analysis. C.P., S.M., A.G., A.B., A.N., R.T., and M.Al. provided human samples, performed immunofluorescence staining, and acquired microscopy images. F.T. provided human samples and gave critical input. Z.L. and F.G. provided critical materials and valuable input. J.A. performed bioinformatics and helped design

figures. P.M.K.G. performed RNA-seq, bioinformatics analysis, and data curation. **Competing interests:** The authors declare that they have no competing interests. **Data and materials availability:** Raw sequencing data have been deposited in the GEO database under GSE226946. Additional sequencing data used are available in the GEO database under GSE136103. The *Lrat^{cre}* mice were kindly provided by R. Schwabe (Columbia University, New York) under a material transfer agreement with the University of Calgary. All data underlying the results are deposited in Dryad ([59](#)). All other data are available in the main text or the supplementary materials. **License information:** Copyright © 2023 the authors, some rights reserved; exclusive licensee American Association for the Advancement of Science. No claim to original US government works. <https://www.science.org/about/science-licenses-journal-article-reuse>

SUPPLEMENTARY MATERIALS

science.org/doi/10.1126/science.abq5202

Figs. S1 to S7

Table S1

Movies S1 to S8

MDAR Reproducibility Checklist

Submitted 13 April 2022; resubmitted 8 March 2023

Accepted 13 July 2023

10.1126/science.abq5202